Examining Biases in Diurnally-Integrated Shortwave Irradiances due to Two- and Four-Stream Approximations in Cloudy Atmosphere

Seung-Hee Ham[1], Seiji Kato[2], and Fred G. Rose[1]

[1]Science Systems and Applications, Inc. (SSAI), Hampton, Virginia, USA

[2]NASA Langley Research Center, Hampton, Virginia, USA

Submitted to Journal of Atmospheric Science

November 2019

Corresponding author address:

Seung-Hee Ham

NASA Langley Research Center

100 NASA Road

Mailstop 420

Hampton, VA23681-2199

E-mail: seung-hee.ham@nasa.gov

Abstract

Shortwave irradiance biases due to two- and four-stream approximations have been studied for the last couple of decades, but biases in estimating Earth's radiation budget have not been examined in earlier studies. In order to quantify biases in diurnally-averaged irradiances, we integrate the two- and four-stream biases using realistic diurnal variations of cloud properties from Clouds and the Earth's Radiant Energy System (CERES) synoptic (SYN) hourly product. Three approximations are examined in this study, delta-two-stream-Eddington (D2strEdd), delta-two-stream-quadrature (D2strQuad), and delta-four-stream-quadrature (D4strQuad). Irradiances computed by the Discrete Ordinates Radiative Transfer (DISORT) and Monte Carlo (MC) methods are used as references. The MC noises are further examined by comparing with DISORT results. When the biases are integrated with a one-day of solar zenith angle variation, regional biases of D2strEdd and D2strQuad reach up to 8 W m^{-2}, while biases of D4strQuad reach up to 2 W m^{-2}. When the biases are further averaged monthly or annually, regional biases of D2strEdd and D2strQuad can reach –1.5 W m^{-2} in SW top-of-atmosphere (TOA) upward irradiances and +3 W m^{-2} in surface downward irradiances. In contrast, regional biases of D4strQuad are within +0.9 for TOA irradiances and –1.2 W m^{-2} for surface irradiances. Except for polar regions, monthly and annual global mean biases are similar, suggesting that the biases are nearly independent to season. Biases in SW heating rate profiles are up to –0.008 Kd^{-1} for D2strEdd and –0.016 K d^{-1} for D2strQuad, while the biases of the D4strQuad method are negligible.

1. Introduction

The integro-differential radiative transfer equation cannot be analytically solved unless a simplifying assumption is made because the radiance leaving to a certain direction is contributed by the multiple scattering components from all directions. To obtain a solution, scattered radiances in the source function are approximated at a limited number of discretized angular directions. The number of angular points is often called the number of streams in the radiation scheme. Even though a higher number of streams gives a better accuracy, the simplified radiation codes such as two- or four-stream approximations (Liou 1974; Joseph et al. 1976; Meador and Weaver 1980; Liou et al. 1988; Chou et al. 1998) have been widely used for reanalysis and general circulation models (GCMs), as well as in the production of radiation budget data, because of efficient computing time (Räisanen 2002; Zhu and Arking 2006; Li et al. 2013).

For the last couple of decades, many studies have investigated the accuracy of two- and four-stream approximations in shortwave (SW) irradiance computations (e.g., Meador and Weaver 1980; King and Harshvardhan 1986; Shibata and Uchiyama 1992; Barker et al. 2003; Halthore et al. 2005; Lu et al. 2009; Hou et al. 2010; Zhang and Li 2013). They performed sensitivity studies with assumed cloud optical depths and solar zenith angles for examining two- and four-stream biases.

The aforementioned findings are valuable, but it is not clear how the two- and four-stream biases influence the estimation of Earth's radiation budget, and if so, how large the magnitude of biases would be. A few studies tried to answer this question. Zhu and Arking (1994) estimated diurnally-integrated biases of the delta-two-stream and four-stream approximations, as functions of latitude and cloud optical depth. However, it is not straightforward to infer the two- and four-stream biases with the realistic variations of the cloud optical depths from their results. In addition, Barker et al. (2015) examined two-stream biases in SW broadband irradiances with clouds derived from A-train space-borne radar and lidar measurements. However, they did not consider diurnal variations of solar zenith angles because A-train satellites only observe a fixed location twice a day. It is expected that the two- and four-stream biases are partly canceled out over the course of a day because the sign of two- and four-stream biases usually changes at a certain solar zenith angle. Even though a smaller magnitude is expected, estimating diurnally-integrated biases is needed to understand the impact of two- and four-stream biases on radiation budget.

Therefore, in this study, we use cloud fields from hourly satellite products to estimate two- and four-stream biases in diurnally-integrated SW irradiances. We expect that the magnitudes and signs of two- and four-stream biases are affected by cloud types, generating variations of biases depending on the region. Therefore, our objective is to provide the global distribution of two- and four-stream biases with realistic cloud fields. As a reference, we consider Discrete Ordinates Radiative Transfer (DISORT) and Monte Carlo (MC) methods. Based upon the references, two- and four-stream biases are estimated for each hourly 1° grid box, and then they are averaged monthly or annually. We obtain absolute biases of SW irradiances (W m^{-2}) instead of relative biases (%) to make it easier to assess the impact on Earth's radiation budget.

2. Methodology

2.1. Radiative transfer models

To compute SW irradiances with two- and four-stream approximations, we use the modified version of the Fu-Liou model (Fu and Liou 1993; Fu et al. 1997) by National Aeronautics and Space Administration (NASA) Langley Research Center; i.e. a flux model of Clouds and the

Earth's Radiant Energy System (CERES) with k-distribution and correlated-k for Radiation (FLCKKR) (Kratz and Rose 1999; Kato et al. 1999, 2005; Rose et al. 2006). We run the Fu-Liou model in three modes; i) delta-two-stream-Eddington (D2strEdd) (Irvine 1968; Kawata and Irvine 1970; Shettle and Weinman 1970), ii) delta-two-stream-quadrature (D2strQuad) (Liou 1992), and iii) delta-four-stream-quadrature (D4strQuad) (Liou et al. 1988; Fu 1991) methods. These three approximations are widely used in the current climate and numerical models, and comprehensive descriptions are provided in earlier studies (e.g., Liou 1974, 1992; Meador and Weaver 1980; Toon et al. 1989). The D2strEdd method assumes $I(\mu,\tau)=I_0(\tau)+\mu I_1(\tau)$, stating that the radiance is expressed by a polynomial of μ along with the zeroth (I_0) and first (I_1) Legendre polynomial moments of the radiance. In the D2strQuad method, the angular integral of the radiance is expressed using the two-point Gaussian quadrature, while the four-point Gaussian quadrature is used for the D4strQuad method. In all D2strEdd, D2strQuad, and D4strQuad methods, a strong forward peak of the phase function is approximated by Dirac delta function (δ function), based on the delta-M scaling method (Wiscombe 1977). Earlier results indicate that the D4strQuad method generally performs better than most two-stream approximation methods (e.g., Zhu and Arking 1994).

As a reference to estimate biases of the D2strEdd, D2strQuad, and D4strQuad approximations, we consider the Discrete Ordinates Radiative Transfer (DISORT) model (Stamnes et al. 1988). The DISORT method uses the discrete ordinate approximation to express the integral term of the source function with Gaussian quadrature, which is similar to the D2strQuad and D4strQuad method. However, the DISORT model is designed for a higher number of streams than these methods. For the higher number of streams, the scattering phase function is expanded with Legendre polynomials and the radiance is expanded with a Fourier cosine series. Then the matrix form is used to solve the radiative transfer equation. The accuracy of the DISORT model increases with the number of streams, but the results converge once the number of streams is ≥ 16 (Appendix A). Therefore, we use DISORT model results with 40 streams to compare with two- and four-stream simulation results.

As another reference, we also use the Intercomparison of 3-D Radiation Code (I3RC) (Cahalan et al. 2005) community Monte Carlo model (Pincus and Evans 2009) with the independent column approximation (ICA) assumption. The principle of the MC method is described in earlier studies (e.g., Barker and Davis 1992, Davis et al 1997) and the short description of the method is following. At the beginning of the model run, photons are injected at top of the domain. When photons reach extinction media such as cloud or gas, photons are either absorbed or scattered based on the specified probability of single scattering albedo. When photons are scattered, the direction of the photons is statistically determined using the cumulative distribution function of the scattering phase function. Photons are tracked until completely absorbed or escape from the domain. By counting the number of photons escaping from the top and bottom boundaries of the domain, reflection and transmittance are determined. The number of absorbed photons in atmospheric layers is used to compute heating rate profiles. To run the I3RC model with all cases at one time, we generate many columns in the domain. With the independent column approximation, only the vertical location of photons is tracked, i.e. the information of horizontal location is lost and thus there is no interaction among columns. Therefore, it is equivalent to having many plane-parallel atmospheres in a domain. Note that the number of photons is distributed proportionally to the cosine of solar zenith angle (μ_0), which is also proportional to the solar incoming irradiance. For example, if we consider ten columns with ten different μ_0 as 0.1, 0.2, 0.3, 0.4, 0.5, 0.6, 0.7, 0.8, 0.9, and 1.0 in the domain, the column with

μ_0 = 1 gets 10 times larger number of photons compared to the column with μ_0 = 0.1. If we input 1000 photons in the domain, the columns mentioned above get 18, 36, 55, 73, 91, 109, 127, 145, 164, and 182 photons, respectively, and their average is 100 photons per column. In other words, the columns with μ_0 = 0.1, 0.2, 0.3, 0.4, 0.5, 0.6, 0.7, 0.8, 0.9, and 1.0 get 0.18, 0.36, 0.55 0.73, 0.91, 1.09, 1.27, 1.45, 1.64, and 1.82 times the average photons per column, respectively. Throughout this study, when we refer to the number of photons for the MC simulation, we use the average number of photons per column in the domain but a smaller weighting is given to the column with a small μ_0, and vice versa.

Note that the MC takes into account the exact scattering phase functions within the resolution of equal probability bins, and thus the method is equivalent to the results with the infinite number of streams in the model simulation (Barker et al. 2015). This means that as long as enough number of streams is used for the DISORT method and enough number of photons is used for the MC method, the two methods should produce almost identical results. We verify this in Appendix A. For generating the look-up table (LUT) using the MC model in Section 2.2, however, we need to limit the number of photons less than 10^6 due to the long computation time. The expected MC noises with 10^6 photons are up to 1 W m^{-2} (Fig. A1). Because the MC noises are randomly distributed, we will examine if the Monte Carlo noises are canceled out in monthly and annual means by comparing with DISORT results in Section 3.2.

2.2. Model inputs

We use common inputs in all radiative transfer methods; D2strEdd, D2strQuad, D4strQuad, MC, and DISORT. Specifically, we consider 18 narrow bands (Rose et al. 2006) for computing gaseous absorption, molecular scattering, cloud scattering, and surface albedo of SW broadband radiation from 0.1754 to 4.0 μm. Aerosol is ignored in this study, and our main focus remains for cloudy atmosphere. The correlated-k distribution method (Kratz and Rose 1999; Kato et al. 1999, 2005) is used to compute the gas absorption optical depth, and the molecular scattering optical depth is computed using a pressure profile (Fu and Liou 1993). In this study, midlatitude summer (MLS), and midlatitude winter (MLW) profiles (McClatchey et al. 1972) are considered, depending on the total precipitable water (PW), as explained in Section 2.3.

Cloud scattering properties such as single scattering albedo, scattering phase function (or asymmetry factor for two- or four-stream approximations), and extinction efficiency are considered for the 18 bands. The scattering parameters for water particles were computed using Mie theory. In addition, ice particles are assumed to be two habit mixtures (THM) and their optical properties are from Liu et al. (2014).

The surface type is assumed to be either ocean, cropland, or snow. The spectral surface albedo for the ocean surface is computed based on Jin et al. (2004), who parameterized the ocean albedo as a function of ocean chlorophyll concentration, near-surface wind speed, atmospheric transmittance, and solar zenith angle. For this study, the wind speed and chlorophyll concentration are fixed at 5 m s^{-1} and 0 mg m^{-3}, respectively. The surface albedo for cropland is fixed at 0.10 for the clear sky, and 0.12 for the cloudy sky. The surface spectral albedo for snow surface is based on Jin et al. (2008) and is a function of snow grain size. The snow grain size = 100 μm is assumed.

Because of the long computation time of the DISORT and MC models (Table 3), it is practically difficult to run the models with a 1-hour temporal resolution and a 1° spatial resolution for computing monthly and annual means. To improve the computational efficiency of the model simulations in this study, a look-up table (LUT) is made for various combinations of surface, atmospheric, and cloud conditions. These include 3 surface type albedos (ocean, land, and snow), 2 atmospheric profiles (MLS and MLW), and 10 values of the cosine of the solar zenith angle from 0.1 to 1.0 with a 0.1 interval. In addition, for clouds, 9 values of cloud optical depth (0.3, 1, 2, 5, 10, 20, 30, 40, and 50), two cloud phases (ice and liquid), 16 values of the cloud top height from 1 to 16 km with a 1-km interval, and 16 values of the cloud base height from 0 to 15 km with a 1-km interval are included, as listed in Table 1. For ice-phase clouds, an effective diameter (d_e) of 65 μm is used, while a 10 μm of effective radius (r_e) is used for liquid-phase clouds. The pre-computed LUT is used for calculating SW irradiances for surface, atmosphere, and cloud conditions obtained from the CERES synoptic (SYN) product (Section 2.3).

Because the consistent spectral bands, surface albedos, atmospheric profiles, and cloud properties are used for the D2strEdd, D2strQuad, D4strQuad, MC, and DISORT methods, differences of two- or four-stream irradiances from the MC/DISORT irradiances are regarded as modeling biases solely due to the two-stream or four-stream approximations. Note that the three-dimensional (3D) radiative effects related to horizontal photon transports or sub-pixel scale variabilities do not contribute to the differences discussed in this study because the independent column and plane-parallel approximations are used for all radiative transfer calculations. Ham et al. (2014) showed that the 3D effects decrease with spatial scales and are negligible for scales greater than 20 km. In addition, SW modeling biases due to partly cloudy pixels are quantified in Ham et al. (2019).

2.3. Computation of SW irradiances using surface, atmosphere, and cloud properties from the CERES SYN product

For obtaining realistic surface, atmospheric, and cloud properties, we use CERES Edition 4A SYN irradiance and clouds hourly product (ASDC 2017, Doelling et al. 2013, Rutan et al. 2015). The CERES SYN product was produced by merging geostationary and polar-orbit satellite measurements. The geostationary satellites include series of Geostationary Operational Environmental Satellite (GOES), Meteosat, and Multi-Functional Transport Satellite (MTSAT), while the polar-orbit satellites include MODIS on Terra and Aqua (Doelling et al. 2013). All geostationary visible and infrared channels are calibrated based on Terra Moderate Resolution Imaging Spectroradiometer (MODIS) radiances (Doelling et al. 2013; Rutan et al. 2015). Cloud properties are derived from MODIS narrow bands using CERES single satellite footprint (SSF) algorithm (Minnis et al. 2011a, b), four times a day, combining two MODIS sensors aboard Terra and Aqua. For the time between Terra and Aqua observations, cloud properties are derived from geostationary satellites (Minnis et al. 1995). The SYN product provides hourly 1°-gridded cloud properties, including cloud top/base heights, cloud phase, and cloud optical depth for four cloud types, where the cloud type is defined by the cloud top pressure; low (> 700 hPa), mid-low (500–700 hPa), mid-high (300–500 hPa), and high (< 300 hPa) clouds. Note that the ice cloud optical depths in Ed4 SYN product were retrieved using the roughened hexagonal scattering database (Yang et al 2008a, b), while all models in this study use more recent two-habit mixture (THM) scattering database (Liu et al. 2014), which will be used for future CERES processing (Edition 5). To avoid modeling errors due to the inconsistent ice scattering databases (Loeb et al. 2018), the ice cloud optical depths derived under the roughened hexagonal scattering database are converted into values under THM scattering database by satisfying $(1 - g_{hex})\tau_{hex} = (1 - g_{THM})\tau_{THM}$, where g_{hex} and τ_{hex} are asymmetry parameter and cloud optical depth retrieved with roughened hexagonal scattering database, respectively, and g_{THM} and τ_{THM} are asymmetry parameter and cloud optical depth retrieved with THM scattering database, respectively. This is based on Similarity theory (van de Hulst 1974).

For each cloud type of 1° grid box, we derive SW irradiances from the LUT with taking into account sub-grid variations of cloud optical depths. In doing so, a gamma distribution is constructed using the linear and logarithmically mean cloud optical depths for each type (Thom 1958; Kato et al. 2005), which are provided in SYN product. Then the integration of irradiances for the gamma distribution is performed using the 9-point Gaussian quadrature, while a similar approach was used in earlier studies (Barker et al. 1996; Ham and Sohn 2010, Ham et al. 2019). Then the gamma-weighted irradiance for each cloud type is weighted by the respective cloud fraction to obtain the irradiance of the hourly grid box:

$$F_{grid} = f_{low}F_{low} + f_{mid-low}F_{mid-low} + f_{mid-high}F_{mid-high} + f_{high}F_{high}$$
$$+\left(1 - f_{low} - f_{mid-low} - f_{mid-high} - f_{high}\right)F_{clr} \ . \qquad (1)$$

Consecutively, the hourly grid-box irradiances are temporarily averaged to obtain monthly or annual means.

In the above processes, the SW irradiance is derived by interpolating the LUT for the given cloud optical depth and cosine of the solar zenith angle (μ_0). We determine whether the LUT is interpolated logarithmically or linearly depending on the range of the cloud optical depth and μ_0, in order to minimize interpolation errors (Appendix B). As a result, the interpolation errors are expected to be < 1 W m^{-2}. Note that the interpolation errors affect results from all radiation methods, and therefore, they do not influence the estimation of two- and four-stream biases.

While the interpolation of the LUT is performed for the cloud optical depth and μ_0, cloud altitudes and atmospheric profiles are truncated and the closest values in the LUT are chosen. For example, cloud top and base heights are truncated with a 1 km interval for choosing irradiances in the LUT. In addition, the MLS atmosphere is used for the precipitable water (PW) > 1 cm, while the MLW is used for PW ≤ 1 cm. Surface types are separated into three types, land, ocean and snow/ice covered surfaces. The surface type of the grid box is determined by ocean (f_{ocn}) and snow/ice coverages (f_{snow}) in the SYN product. The rest of ocean and snow/ice coverages is considered as a land coverage ($f_{lnd} = 1 - f_{ocn} - f_{snow}$). If the grid box consists of more than one surface type, the irradiances are computed for each surface type, and these are weighted by the coverages:

$$F_{grid} = f_{ocn}F_{ocn} + f_{land}F_{land} + f_{snow}F_{snow} \qquad (2)$$

where F_{ocn}, F_{land}, and F_{snow} are the computed SW irradiances for ocean, land, and snow surface types, respectively.

Even though the geostationary visible and infrared channels are calibrated against MODIS (Doelling et al. 2013; Rutan et al. 2015), discontinuities at the geostationary satellite boundaries in the CERES SYN product are apparent (ASDC 2017). These discontinuities are smoothed by the constraining algorithm in the downstream CERES Energy Balanced And Filled (EBAF) process (Rose et al. 2013, Kato et al. 2013, 2018a), in which atmosphere and cloud conditions are adjusted to give better consistency in LW and SW top-of-atmosphere (TOA) irradiances to actual TOA observations. However, the adjusted cloud properties are not available in the CERES SYN product, and we use initial cloud properties obtained from multiple satellites in this study. This means that the discontinuities across the geostationary satellites will appear in computed SW irradiances in this study (Fig. 9). However, the impact of discontinuities on the model-to-model differences is negligible, as shown in the next section (Figs. 10, 11).

3. Results

3.1. Biases of the two- and four-stream approximation for the simplified cloud cases

In this section, we estimate biases by the D2strEdd, D2strQuad, and D4strQuad methods for selected cloud cases. Figure 1 shows biases for water clouds located at 2–3 km altitudes over ocean as a function of the cosine of the solar zenith angle (μ_0 = cos θ_s) and cloud optical depth (τ_c) for the MLS atmosphere. Biases by the D2strEdd, D2strQuad, and D4strQuad methods for the MLW atmosphere (not shown) are very similar to those shown in the MLS atmosphere, and we only show the results for the MLS atmosphere in this section. Biases of the D2strEdd (Fig. 1a–c) and D2strQuad (Fig. 1e–g) methods are quite similar. The sign of D2strEdd and D2strQuad methods in TOA upward SW irradiances are mostly negative. The sign of biases in surface downward SW irradiances is opposite to the sign of TOA biases, consistent with results in earlier studies (e.g., Meador and Weaver 1980; Zhu and Arking 1994; Lu et al. 2009; Zhang et al. 2012; Barker et al. 2015). In contrast, the D4strQuad method produces positive biases in TOA upward irradiances and negative biases in surface downward irradiances (Fig. 1i–k), with a smaller magnitude compared to the D2strEdd or D2strQuad method (Zhu and Arking 1994).

Figure 1 also shows that, for a given cloud optical depth (τ_c), the sign of the irradiance bias often changes when the cosine of the solar zenith angle (μ_0) changes. This means that the biases are partly canceled when we integrate the biases over the course of the day. To examine this feature, we use three examples of the diurnal cycle of μ_0 in Fig. 2. These are chosen at three latitude regions (0.5°N, 30.5°N, and 60.5°N) on 15th October 2010. With these three diurnal cycles, the SW bias is integrated by,

$$\Delta F(\tau_c) = \frac{1}{24}\int_0^{24} \Delta F(\mu_0(h), \tau_c)\, dh \quad (3)$$

where $\Delta F(\mu_0, \tau_c)$ is the bias as a function of μ_0 and τ_c obtained in three left columns in Fig. 1, and $\mu_0(h)$ is the cosine of solar zenith angle for the given hour (h) in Fig. 2. The diurnally-integrated biases are shown in the fourth column of Fig. 1. As expected, the diurnally-integrated bias [$\Delta F(\tau_c)$] is generally smaller than the instantaneous bias [$\Delta F(\mu_0, \tau_c)$]. For example, $\Delta F(\tau_c)$ of the D2stEdd bias in TOA SW upward irradiances is up to –5 W m^{-2} (blue lines, Fig. 1d), while $\Delta F(\mu_0, \tau_c)$ is up to –8 W m^{-2} (Fig. 1a). Note that the overall shape of $\Delta F(\tau_c)$ remains very similar for the three different diurnal cycles of μ_0 [$\mu_0(h)$] – shown by solid, dashed, and dotted lines in Fig. 1d. In the examples of the diurnal integration in Fig. 1, it is assumed that the cloud optical depth remains the same over the course of the day, but in Section 3.2, diurnal variations of both μ_0 and τ_c will be considered using the CERES SYN product for the integration.

The diurnally-integrated biases for the D2stQuad method [$\Delta F(\tau_c)$] have different signs depending on τ_c (Fig. 1h), while the biases of D2strEdd (Fig. 1d) and D4strQuad (Fig. 1l) have the same sign for all ranges of τ_c. This suggests that there will be larger cancellations of the D2stQuad biases compared to the D2strEdd or D4strQuad method when averaging the biases monthly or annually.

In Figs. 1m–t, MC simulation results with 10^6 and 10^8 photons, hereafter referred to as MC1M and MC100M, respectively, are compared to DISORT simulation results. The differences between MC1M and DISORT (Figs. 1m–p) or MC100M and DISORT (Figs. 1q–t) are much smaller than the biases of the D2strEdd, D2strQuad, or D4strQuad methods (Figs. 1a–l), demonstrating the robustness of both MC and DISORT methods. However, MC1M results show larger random noises, compared to the MC100M results (Appendix A).

The signs of D2strEdd, D2strQuad, D4strQuad biases for ice clouds are similar to those found in water clouds (Fig. 1), but there are also subtle differences mostly due to different scattering phase functions. For example, the D2strEdd method produces positive biases in atmosphere-absorbed irradiance for $\mu_0 > 0.8$ for water clouds (Fig. 1b), but the biases are positive for $\mu_0 > 0.6$ for ice clouds (Fig. 3b).

While the biases of the D2strEdd, D2strQuad, D4strQuad methods over ocean and land (not shown) are similar, the biases over snow are quite different. In Fig. 4, both D2strEdd and D2strQuad methods produce much larger magnitudes of biases in surface downward irradiances over snow (Figs. 4c, g) compared to the biases for the ocean surface type (Figs. 1c, g). This suggests that the two-stream biases are significant during summer in polar regions and the use of higher-stream models is desirable.

The computed SW heating rates from the D2strEdd, D2strQuad, and D4strQuad methods are compared with those from the MC method in Figs. 5 and 6, for water and ice clouds, respectively. For clear skies, SW heating rate biases are very small (0.02 K d^{-1}) for all altitudes and are not provided here. In the comparison shown in Fig. 5, we use a water cloud layer with cloud optical depth = 10, particle effective radius = 10 μm, cloud base height = 2 km, and cloud top height = 3 km. Large biases of the D2strEdd, D2strQuad, and D4strQuad occur at the altitude where the cloud layer is present (2–3 km, gray areas in Fig. 5). The SW heating rate bias is negative for D2strEdd and D2strQuad methods at 2–3 km altitude, while the D2strQuad bias is larger negative than the D2strEdd bias. This is consistent with those found in earlier studies (e.g., Lu et al. 2009). In contrast, the SW heating rate bias by the D4strQuad method is generally positive and the magnitude is smaller compared to D2strEdd and D2strQuad biases. Below 2 km, the D2strEdd and D2strQuad SW heating rate biases are positive, while the magnitude of the positive D2strEdd bias is larger than the D2strQuad bias. The results suggest that both D2strEdd and D2strQuad methods underestimate the cloud absorption and overestimate the cloud transmission, consistent with the results shown in Fig. 1. The MC method with 10^6 and 10^8

photons (MC1M and MC100M) produces non-systematic differences from the DISORT results, while MC1M generates larger random noises than MC100M.

In Fig. 6, we use ice clouds with cloud optical depth = 10, particle effective diameter = 65 μm, cloud base height = 10 km, and cloud top height = 12 km. Similar to the comparison of water cloud heating rates (Fig. 5), large differences in SW heating rates occur at the altitude of ice cloud layers (10–12 km, gray areas in Fig. 6). Both D2strEdd and D2strQuad methods underestimate SW heating rates at 10–12 km and overestimate SW heating rates below 10 km. Compared to water clouds (Fig. 5), the magnitude of SW heating rate biases for ice clouds (Fig. 6) is larger, because the SW heating rate is inversely proportional to air density ($\propto 1/\rho_{\mathrm{air}} \times \Delta F/\Delta z$) and the air density decreases with altitude.

From the sensitivity tests in Figs. 1–6, except over snow surfaces, it is expected that the D2strEdd and D2strQuad methods are likely to cause negative biases in TOA SW upward irradiances, and positive biases in surface SW downward irradiances. In contrast, the D4strQuad method tends to introduce positive biases in TOA SW upward irradiances and negative biases in surface downward irradiances with a smaller magnitude. The specific signs and magnitudes depend on cloud optical depth, cloud phase, cloud altitude, solar zenith angle, and surface type. In the following two sections, we integrate the biases of the three approximated methods using the CERES SYN hourly product.

3.2. Diurnally-integrated biases of the delta-two-stream-Eddington (D2strEdd), delta-two-stream-quadrature (D2strQuad), and delta-four-stream-quadrature (D4strQuad) methods

In this section, we estimate diurnally-integrated monthly and annual biases in SW irradiances using surface, atmosphere, and cloud properties from the one-year (2010) of the CERES

SYN1deg-hour product. Figure 7 shows monthly mean total cloud amount, cloud optical depth, snow coverage, and total precipitation water for January and July 2010. The cloud properties are averaged for four cloud types – high, mid-high, mid-low, and low clouds – weighted by respective cloud fractions. Both months show large cloud amounts over the southern and northern hemisphere storm-track regions (Figs. 7a, 7b), whereas locations of deep convective clouds over the Warm Pool slightly change depending on the two seasons. The large cloud optical depths occur over the Warm Pool and storm-track regions (Fig. 7c, 7d). The snow cover over Antarctica is 100% for both seasons, while the snow cover over the Arctic is close to 100% for winter time, and 60–80% for summer time (Figs. 7e, 7f). In addition, the precipitable water is large over regions where deep convections occur (Figs. 7g, 7h).

To examine vertical distributions of cloud layers, we compute volume cloud coverage profiles (%) using cloud top and base heights from the CERES SYN product in the following process. First, for the given cloud base and top heights of each cloud type of each 1° grid box, we compute the volume cloud coverage profile for 126 vertical bins defined from 0 to 20 km with a 0.16 km interval. Second, we average the volume cloud coverage profiles for four cloud types for each 1° grid box based on cloud amounts of the four cloud types. Third, we average the profiles temporally and zonally to get monthly means, as shown in Figs. 8a and 8b. In these figures, abundant high clouds over the tropics and low clouds in high-latitude regions are captured in both seasons. Because we register cloud top and base heights to the nearest boundary of 1-km interval in applying to the look-up-table (LUT) (Section 2.3), we apply the same process to produce cloud coverage profiles shown in Figs. 8c and 8d. This process does not change cloud profiles significantly so that most features in the original vertical resolution remain.

Because SW irradiances are computed with the LUT generated by the simplified surface, atmosphere, and cloud properties, resulting irradiances are different from those computed with original properties. To examine the feasibility of our approach, TOA SW irradiances computed with the simplified properties are compared with CERES SYN observed SW irradiances in Fig. 9. The large differences between simulations and observations are shown over the desert, deep convective clouds, and polar regions (Figs. 9e, 9f). The large biases over the desert and polar regions are likely due to the simplifying assumption of the surface albedo. The positive modeling biases over deep convective clouds in Figs. 9e, 9f might be related to constructing a gamma distribution for large cloud optical depth values. This is because there is a larger deviation from the gamma function for a larger standard deviation. Except for those regions, the simulated and observed irradiances agree to within 4 W m^{-2}.

Note that the simulated results from DISORT and D4strQuad (Figs. 9e and 9f versus Figs. 9g and 9h) show very similar biases compared to the observations. This suggests that the biases shown in Figs. 9e–h are not due to the radiation method but from other parameters such as land surface albedos, cloud optical depths, and gamma functions mentioned above. Note that our simulated irradiances from the LUT (Figs. 9e–h) quite resemble the computed irradiances from CERES SYN product (Figs. 9i, j) except land regions, demonstrating feasibility of the LUT approach. In Figs. 9e–h, discontinuities are shown along the longitudes around 120°E and 60°W, due to cloud discontinuities at the boundaries of geostationary satellites (Section 2.3). A similar pattern is shown for the differences between SYN computed irradiances and observed irradiances (not shown).

From the comparison between simulated and observed SW irradiances, we conclude that our modeling approach has larger uncertainties over land regions compared to ocean regions due to the surface albedo assumption. However, even though the impact of the surface albedo on the SW irradiance is significant, the impact of the surface albedo on the two- and four-stream biases is much smaller, as discussed in Appendix C.

Figure 10 shows the biases due to two- and four-stream assumptions in monthly and annual means. In this figure, DISORT simulation results are used as references to quantify biases of the D2strEdd, D2strQuad, and D4strQuad methods. As discussed in Section 3.1, the D2strEdd and D2strQuad methods produce negative biases in TOA irradiances over cloudy regions, up to –1.5 W m^{-2}, while the magnitude of the biases of the D2strEdd method is larger than that of the D2strQuad method. This is because the D2strQuad method produces negative biases for optically thin clouds ($\tau < 10$) and positive biases for optically thick clouds ($\tau > 20$) (Figs. 1g, 1h, 3g, and 3h), causing partial cancellations in monthly and annual means, as discussed in Section 3.1. Over polar regions, the D2strQuad method shows large positive differences in Figs. 10d–f, as also shown in Figs. 4e and 4h.

Compared to the D2strEdd and D2strQuad methods, the D4strQuad method shows smaller regional biases in TOA SW irradiances up to +0.9 W m^{-2} (Figs. 10g–i). Global annual means of SW TOA upward irradiance biases (the third column of Fig. 10) are –0.57, –0.15, and +0.32 W m^{-2} for the D2strEdd, D2strQuad, and D4strQuad methods, respectively. Global mean biases by the D2strQuad method are smaller than global mean biases by the D4strQuad method due to the cancellation of positive biases over polar regions and negative biases over cloudy regions. The MC1M method shows quite good agreements with DISORT results, and the regional differences are < 0.3 W m^{-2}, and the global mean difference is +0.04 W m^{-2}. This suggests that most of MC noises are smoothed out in monthly and annual means. In all methods, monthly and annual mean biases are quite similar, except for polar regions.

When the TOA SW biases are separated by ocean and land regions (Table 2), larger biases occur over ocean. This is because the occurrence of cloudy skies is higher over ocean, and the biases due to two-stream or four-stream approximations are larger in cloudy skies, compared to clear skies.

Biases in surface downward irradiances shown in Fig. 11 are larger than biases in TOA upward irradiances. The sign of the biases is positive in the D2strEdd and D2strQuad methods and negative in the D4strQuad method, which is consistent with the results discussed in Section 3.1. The biases in the D2strEdd and D2strQuad methods are up to 3 W m^{-2} regionally, and global annual mean biases are +0.98 and 1.90 W m^{-2}, respectively. In contrast, D4strQuad biases are regionally up to –1.2 W m^{-2} and the global annual mean is –0.56 W m^{-2}. Except for polar regions, monthly and annual global mean surface irradiance biases are very similar to each other, which is also found in TOA upward irradiances. Compared to land regions, larger biases in surface irradiances occur over ocean (Table 2) due to a similar reason in TOA upward irradiances.

Figure 12 shows the biases of SW heating rates computed by the three methods. The D2strEdd (Figs. 12d–f) and D2strQuad (Figs. 12g–i) methods produce negative biases in SW heating rates at 8–12 km over the tropics and 0–8 km in midlatitude to high-latitude regions. The magnitude of the D2strQuad method is larger (up to –0.016 K d^{-1}) than that of the D2strEdd method (up to –0.008 K d^{-1}), as also shown in Figs. 5 and 6. In addition, the D2strEdd method (Figs. 12d–f) produces positive SW biases below 1 km, which is consistent with Figs. 5 and 6. Compared to the D2strEdd and D2strQuad methods, the D4strQuad method (Figs. 12j–l) produces very small biases in SW heating rates, less than 0.004 K d^{-1}. MC results also agree well with DISORT results to within 0.004 K d^{-1} (Figs. 12m–o), suggesting that MC noises are mostly canceled in monthly and annual means.

4. Discussions

In this study, due to the long computation time of MC and DISORT models, we minimized the size of look-up-table (LUT). During the process, we simplified the cloud particle size, atmospheric profiles, and land surface albedo. The impact of assumptions of the cloud particle size, atmospheric profile, and land surface albedo on the two- and four-stream biases is examined in Appendix C. It is shown that the impact of the particle size, water vapor profile, and land surface albedo on the diurnally-integrated biases is within 0.17 W m^{-2}, 0.24 W m^{-2}, and 0.61 W m^{-2}, respectively. The impact of these parameters is one-order smaller than the impact of cloud optical depth, considering the biases change easily up to 2–8 W m^{-2} depending on the cloud optical depth (fourth columns of Figs. 1, 3, 4, C2, C3, and C4). This justifies our approach that the two- and four-stream biases are estimated for specific cloud optical depths and solar zenith angles, while the crude assumption is made for the cloud particle size, land surface albedo, and water vapor profile. If we implement a more accurate cloud particle size, land surface albedo, and water vapor profile, the overall magnitude of the biases can be slightly shifted, and this is left for future examinations.

In this study, irradiances computed by DISORT and MC are used for the reference. While these models produce accurate irradiances, the accuracy comes with a computational cost. In Table 3, the computing time from various radiation methods is estimated for the same set of input cases. D2strEdd and D2strQuad are the fastest methods among them. The computing time of the D4strQuad method is 1.7 times longer than that of D2strEdd, but it is still much faster than the DISORT or MC method. In contrast, the MC method with 10^8 photons is most computationally expensive. In Appendix A, it is shown that DISORT results converge once the number of streams ≥ 16, while MC results are not completely converged with 10^8 photons. Therefore, it seems that the DISORT method is generally more efficient than the MC method. However, messaging passing interface (MPI) parallel programming is not used for running MC model in this study. If the MPI is implemented, the computing time for the MC method can be significantly improved.

The cloud properties used in this study were obtained from passive sensors from geostationary and polar-orbiting satellites, while active sensors such as CALIPO or CloudSat in A-train mission can give more accurate cloud height information particularly for multiple cloud layers (Kato et al. 2018b). However, active sensors on A-train satellite observations are limited to twice a day, which do not provide diurnal variations of clouds. From the comparison between passive-derived only and active-passive combined cloud properties for the consistent temporal sampling (Kato et al. 2018b), it was shown that cloud top heights of deep convective clouds over the tropics are too low, and cloud top heights of southern hemisphere storm-track clouds are too high in passive sensor measurements. Therefore, this suggests that the negative SW heating rate biases by the D2strEdd and D2strQuad methods, shown at 8–12 km over the tropics (Fig. 12), might be shifted upward if we implement more accurate cloud height derived from active sensors. In addition, the negative biases shown in the southern storm-track clouds will be shifted towards the surface. However, the SW TOA and surface irradiances are less sensitive to cloud vertical distributions in comparison to heating rate profiles, and thus the two- and four-stream biases in the TOA and surface irradiances shown in this study should not be affected by cloud height errors.

In this study, we considered up to four cloud types in 1° grid box without taking into account overlapping clouds. This is different from the operational CERES SYN algorithm, where a random overlap assumption is used (Kato et al. 2019). The primary reason why we did not use the overlap assumption is the long computing time for MC and DISORT methods because we need to include all combinations of overlapping cloud scenarios for up to four layers in the LUT. If we consider the overlapping clouds, it would increase each cloud fractions. However, the column-integrated cloud optical depth would remain the same, as identified by passive-sensor retrieved values. This means that the estimated two- and four-stream biases at TOA and surface irradiances are less impacted by the overlapping assumption, in a similar context to the previous paragraph.

5. Conclusions

We estimated the biases in diurnally integrated TOA and surface SW irradiances caused by delta-two-stream-Eddington (D2strEdd), delta-two-stream-quadrature (D2strQuad), and delta-four-stream-quadrature (D4strQuad) approximations using satellite measurements of the surface, atmosphere, and cloud properties. We generated a look-up-table (LUT) with the pre-defined surface, atmosphere, and cloud conditions and integrate the biases using the CERES Edition 4A SYN data product.

The instantaneous and diurnally-integrated biases of the D2strEdd and D2strQuad methods are 2–4 times larger than those found in the D4strQuad method (Fig. 1, 3, and 4). However, the D2strQuad method produces different signs in the biases depending on the cloud optical depth, and as a result, the biases are largely canceled in monthly and annual means (Figs. 10 and 11). Nevertheless, the D4strQuad method generally produces a smaller bias than the biases produced by D2strEdd and D2strQuad methods. In addition, the bias of the D4strQuad method shows a smaller spatial variability compared to the D2strEdd and D2strQuad methods. Compared to ocean or land regions, the D2strEdd and D2strQuad methods produce particularly large biases in surface downward irradiances over snow, and as a result, the monthly regional bias can be as large as 4 W m^{-2} during summer time over polar regions. The results of this study underscore the advantage of the four-stream approximation compared to two-stream approximations in computing daily, monthly, and annual mean irradiances for radiation budget estimates.

Acknowledgement

The work is supported by NASA CERES project. CERES Edition 4A SYN hourly data were downloaded from the NASA Langley Research Center CERES ordering tool at http://ceres.larc.nasa.gov/.

Appendix A: Monte Carlo (MC) noises

The Monte Carlo (MC) method does not approximate the scattering phase function, and thus it is generally considered as truth to assess other approximated radiative transfer methods. However, the MC method uses a statistical approach to determine 1) whether the photon is absorbed or scattered by the media (e.g., clouds) based on the single scattering albedo 2) the direction of the scattered photon based on the cumulative function of the scattering phase function. The magnitude of random noises of the MC method is determined by the number of photons used for computations. The Monte Carlo noise is inversely proportional to the square root of the number of photons ($\propto 1/\sqrt{N_p}$) (Evans and Marshak 2005; Barker et al. 2015) because the variance of the sampling distribution equals the variance of the population divided by the sampling size.

As an alternative way, the I3RC MC model provides a standard deviation of radiative quantities from grouped batches of photons, which can be used as uncertainties of the MC method. The standard deviation of the SW irradiances is obtained as:

$$\sigma_{Batch} = \sqrt{\frac{1}{N_B - 1}\sum_{i=1}^{i=N_B}(F_i - F)^2} \qquad \text{(A1)}$$

where N_B is the number of batches, F_i is the mean of the SW irradiance for the ith batch, and F is the mean of irradiances including all batches, i.e.:

$$F = \frac{1}{N_B}\sum_{i=1}^{i=N_B} F_i \ . \qquad \text{(A2)}$$

The smaller σ_{Batch} means a small deviation of irradiance outputs among batches, indicating a smaller uncertainty of the MC results. We consider 100 batches (each batch contains N_p/100 photons where N_p is the total number of photons) and obtain σ_{Batch} in Fig. A1a–d. Compared to the simulation results with 10^6 photons (MC1M) in Figs. A1a and b, the results with 10^8 photons

(MC100M) in Figs. A1c and d show a one-order magnitude smaller σ_{Batch}. In both simulation results, σ_{Batch} generally increases with a cosine of solar zenith angle (μ_0) simply because an incoming solar irradiance increases with μ_0. For fixed μ_0, the largest σ_{Batch} appears when the cloud optical depth is around 10. This is because the SW irradiances become less sensitive to the cloud optical depth for the cloud optical depth > 10. In Figs. A1e and A1f, values of F from 10^6 and 10^8 photons are compared. For all solar zenith angles and cloud optical depths, the differences in F are randomly distributed and the magnitudes of them are < 1.0 W m^{-2} for TOA upward and surface downward irradiances.

Since the largest σ_{Batch} is shown for $\mu_0 = 1$ and cloud optical depth around 10 in Figs. A1a–d, σ_{Batch} is estimated with various numbers of photons for the fixed μ_0 (=1) and cloud optical depth τ_c (= 10) in Figs. A2a–b. The standard deviation of SW irradiances (σ_{Batch}) rapidly decreases with the number of photons, particularly from 10^4 to 10^6 photons. In Fig. A2c–d, the mean irradiances (F) are provided for various photon numbers with black symbols. In this figure, F with 10^4 photons is deviated from F with 10^8 photons by 9 W m^{-2} for TOA upward SW irradiances (Fig. A2c) and by 15 W m^{-2} for surface downward SW irradiances (Fig. A2d). The SW irradiance differences between 10^6 and 10^8 photons are within 1 W m^{-2}, consistent with Figs. A1e–f. In Figs. A2c–d, the DISORT simulation results with various numbers of streams (red symbols) are also compared with the MC results (black symbols). DISORT produces almost constant values of irradiances with increasing number of streams. For the number of streams $\geq$ 16, the irradiances are within < 0.01 W m^{-2} among different numbers of streams. This indicates that high accuracy can be achieved if the number of streams $\geq$ 16 is used in the DISORT model. In comparison to the DISORT results, MC results with 10^8 photons are still off by 0.5 W m^{-2} for TOA SW irradiances and 1 W m^{-2} for surface downward irradiances due to MC noises. From these comparison results, the DISORT method with 40 streams is used as a reference to obtain modeling biases of D2strEdd, D4strQuad, and D4strQuad methods.

Appendix B: Interpolation of the look-up-table (LUT) for the given cosine of solar zenith angle (μ_0) and cloud optical depth (τ_c)

In this study, the interpolation of the LUT is performed to obtain SW irradiances for the given cosine of solar zenith angle (μ_0) and cloud optical depth (τ_c). If the SW irradiance perfectly follows a linear or logarithmic function with μ_0 or τ_c, the interpolation would not introduce errors. However, the SW irradiance does not follow a linear or logarithmic function perfectly.

In Fig. B1, the interpolation errors are estimated for TOA SW irradiances when a linear-scale (the first row) or logarithmic-scale (the second row) interpolation is performed over μ_0 (left column) or over the cloud optical depth τ_c (right column). The linear interpolation generally works better than the logarithmic interpolation over μ_0 (Fig. B1a versus B1c) except for $\mu_0 \geq 0.5$. Therefore, we apply the linear interpolation for $\mu_0 < 0.5$ and the logarithmic interpolation for $\mu_0 \geq 0.5$, and the corresponding interpolation errors are computed in Fig. B1e. The errors in Fig. B1e is only for $\tau_c = 10$, and interpolation errors for all ranges of cloud optical depths are 0.09±0.66 W m^{-2} with a 68% confidence level.

When the interpolation is performed over the cloud optical depth (τ_c), the linear interpolation causes negative errors in TOA SW irradiances for $\tau_c > 2$ (Fig. B1b). In contrast, the logarithmic interpolation introduces positive errors for $\tau_c < 10$ (Fig. B1d). To minimize the interpolation errors, we combine the linear and logarithmic interpolations depending on the range of τ_c as follows and the corresponding errors are given in Fig. B1f.

$$F = F_{\text{lin}} \qquad \text{for } \tau_c < 2 \qquad \text{(B1)}$$

$$F = 0.7\, F_{\mathrm{lin}} + 0.3\, F_{\mathrm{log}} \qquad \text{for } 2 \le \tau_c < 5 \qquad \text{(B2)}$$

$$F = 0.4\, F_{\mathrm{lin}} + 0.6\, F_{\mathrm{log}} \qquad \text{for } 5 \le \tau_c < 10 \qquad \text{(B3)}$$

$$F = F_{\mathrm{log}} \qquad \text{for } \tau_c \ge 10 \qquad \text{(B4)}$$

Where F_{lin} is the irradiance obtained from the linear interpolation and F_{log} is the irradiance obtained from logarithmic interpolation for the given τ_c. The errors in Fig. B1f is only for $\mu_0 = 1$, and when including all ranges of solar zenith angles, the interpolation errors are –0.52 ± 0.60 W m^{-2} with a 68% confidence level. Note that the interpolation errors shown in this section are included in all simulation results of the D2strEdd, D2strQuad, D4strQuad, MC1M, MC100M, and DISORT methods, and thus the model-to-model differences are not affected by the interpolation errors.

Appendix C: Impacts of the assumptions made for cloud particle size, water vapor profile, and land surface albedo on the estimation of two- and four-stream biases

In this study, the cloud particle size is fixed at 10 μm for water clouds and 65 μm for ice clouds. Since the SW absorption increases with increasing cloud particle size, a different particle size may alter estimated two- and four- stream SW biases. However, if all radiation models show similar behaviors of SW irradiance to the change of the cloud particle size, the two- and four-stream biases would not be much affected by the assumption of the particle size. To examine the impact of water particle size on the biases, in Fig. C1, the biases are estimated for various ice particle effective diameters (d_e) and cosine of solar zenith angles (μ_0) with the fixed cloud optical depth = 10 (first to third columns in Fig. C1). It is shown that the biases change with μ_0 (along the horizontal axes of Fig. C1), but the biases remain almost the same with d_e (along the vertical axes of Fig. C1), suggesting that the SW biases are not sensitive to d_e. As a result, when the biases are diurnally integrated using the three examples of diurnal variations of μ_0 in Fig. 2 with Eq. (3), the diurnally-integrated SW biases are almost constant with d_e (fourth column, Fig. C1).

In Fig. C2, using the three examples of diurnal variations of μ_0 in Fig. 2, the diurnally-integrated SW biases are computed as a function of the cloud optical depth for three different ice particle sizes as d_e = 40, 65, and 80 μm. The values of 40 μm and 80 μm are considered as minimum and maximum of observed ice effective diameters based on the annual statistics from Ed4 SYN hourly product in 2010; the mean and standard deviation of d_e are 60.6 μm and 18.8 μm, respectively. As the ice particle size (d_e) changes, the diurnally-integrated biases at TOA upward, atmosphere-absorbed, and surface downward irradiances change by up to 0.17 W m^{-2}, as summarized in Table C1. The bias changes due to the water particle size (r_e) are slightly larger than those with d_e, but different signs occur depending on the range of r_e (Table C1).

In Fig. C3, we obtain similar plots to Fig. C2 but with changing water vapor profiles in order to examine the impact of the water vapor profile on the estimation of the two- and four-stream biases. In this examination, we scale MLS water vapor profile by 0.1, 1, and 2, which corresponds to the PW values of 0.3, 2.97, and 5.87 cm, respectively, and the results are given in three columns in Fig. C3. Note that the PW of 0.3 cm and 5.87 cm are considered as minimum and maximum of PW, considering total precipitable waters (PWs) for standard tropical (TRO), MLS, MLW, subarctic summer (SAS), and subarctic winter (SAW) are 4.19, 2.97, 0.86, 2.11, and 0.42 cm, respectively. In addition, according to the one-year of Ed4 SYN hourly product in 2010, the mean and standard deviation of PW are 1.90 cm and 1.66 cm, respectively. In Fig. C3, as the water vapor profile changes, the diurnally-integrated biases in atmosphere-absorbed slightly increase, and the biases of surface downward slightly decrease. Note that we use MLW profiles for dry conditions with PW $\leq$ 1 cm and MLS profiles for humid conditions with PW >1 cm when estimating two and four-stream biases (Section 2.1). Therefore, we obtain the bias changes when the PW is changing from 0.3 cm to 0.86 cm (MLW), or the PW is changing 2.97 cm (MLS) to 5.87 cm in Table C1. The overall changes of the biases due to the PW changes are smaller than 0.24 W m^{-2}.

Lastly, the impact of land surface albedo (α_s) is examined in Fig. C4, by comparing the diurnally-integrated biases for three land surface albedos as 0.1, 0.2, and 0.36. Note that the land surface albedos of 0.1 and 0.12 are used in estimating two- and four-stream biases for clear and cloudy skies, respectively. Considering the brightest land albedo occurs over desert and a typical albedo of desert is around 0.36 (Coakley 2003), α_s = 0.36 is used as a maximum value for the sensitivity test. When the land surface albedo changes from 0.1 to 0.36, the biases in diurnally-integrated irradiances change up to 0.61 W m^{-2} (Table C1).

It should be noted that the two- and four-stream biases for clear skies are much smaller than those for cloudy skies. For example, in Fig. C4, the clear-sky biases remain near-zero values with changing land surface albedo (see converged lines for $\tau_c = 0$). Considering that cloud amounts over land are smaller than 40%, we expect that the actual impact of land surface albedo would be smaller than the numbers found in Table C1, which was computed for all range of cloud optical depths. However, further study is desired with a more sophisticated land surface bidirectional model with taking into account spectral dependency.

This section only examines albedo changes over land regions except for snow regions. For the particularly bright snow surface, the biases can be significantly different from those estimated over land, also shown in Fig. 4. We used the snow albedo model of Jin et al. (2008) for this study, with a fixed snow grain size at 100 μm. The snow grain size should be affected by meteorological conditions and seasons, and therefore it is also desired to adopt the season-dependent snow albedo model in the future.

References

ASDC, 2017: CERES SYN 1deg Ed4A Data Quality Summary. NASA Langley Research Center, 36pp, [Available at https://ceres.larc.nasa.gov/documents/DQ_summaries/CERES_SYN1deg_Ed4A_DQS.pdf].

Barker, H. W. and J. A. Davis, 1992: Cumulus cloud radiative properties and the characteristics of satellite radiance wavenumber spectra. *Remote Sens. Environ.*, **42(1)**, 51–64, https://doi.org/10.1016/0034-4257(92)90067-T.

——, 1996: Parameterization for computing grid-averaged solar fluxes for inhomogeneous marine boundary layer clouds. Part I: Methodology and homogeneous biases. J. Atmos. Sci., 53, 2289–2303.

——, and Coauthors, 2003: Assessing 1D atmospheric solar radiative transfer models: Interpretation and handling of unresolved clouds. *J. Climate*, **16,** 2676–2699.

——, J. N. S. Cole, J. Li, B. Yi, and P. Yang, 2015: Estimation of errors in two-stream approximations of the solar radiative transfer equation for cloudy-sky conditions. *J. Atmos. Sci.*, **72**, 4053–4074, https://doi.org/10.1175/JAS-D-15-0033.1.

Cahalan, R. F., and Coauthors, 2005: THE I3RC: Bringing together the most advanced radiative transfer tools for cloudy atmospheres. *Bull. Amer. Meteor. Soc.*, **86,** 1275–1293.

Chou, M.-D., M. J. Suarez, C.-H. Ho, M. M.-H. Yan, and K. T. Lee, 1998: Parameterizations for cloud overlapping and shortwave single-scattering properties for use in general circulation and cloud ensemble models. *J. Climate*, **11**, 202–214, https://doi.org/10.1175/1520-0442(1998)011<0202:PFCOAS> 2.0.CO;2.

Coakley J., 2003: Reflectance and albedo, surface. *Encyclopedia of the Atmosphere*. Academic Press, Cambrigde, MA, USA, pp. 1914–1923.

Davis, A., A. Marshak, R. F. Cahalan, and W. J. Wiscombe, 1997: The Landsat scale break in stratocumulus as a three-dimensional radiative transfer effect: Implications for cloud remote sensing. *J. Atmos. Sci.*, **54**, 241–260.

Doelling, D. R., and Coauthors, 2013: Geostationary enhanced temporal interpolation for CERES flux products. *J. Atmos. Oceanic Technol.*, **30**, 1072–1090, https://doi.org/10.1175/JTECH-D-12-00136.1.

Evans, K. F. and A. Marshak, 2005: *Numerical methods. Three-Dimensional Cloud Structure and Radiative Transfer*. A. Marshak and A. Davis, Eds., Springer-Verlag, 243–281.

Fu, Q., 1991: *Parameterization of radiative processes in vertically inhomogeneous multiple scattering atmospheres*. Ph.D. dissertation, University of Utah, 259 pp.

——, and K.-N. Liou, 1993: Parameterization of the radiative properties of cirrus clouds. *J. Atmos. Sci.*, **50**, 2008–2025, https://doi.org/10.1175/1520-0469(1993)050<2008:POTRPO>2.0.CO;2.

——, K. Liou, M. Cribb, T. Charlock, and A. Grossman, 1997: On multiple scattering in thermal infrared radiative transfer. *J. Atmos. Sci.*, **54**, 2799–2812, https://doi.org/10.1175/1520-0469(1997)054<2799:MSPITI>2.0.CO;2.

Halthore, R. N., and Coauthors, 2005: Intercomparison of shortwave radiative transfer codes and measurements. *J. Geophys. Res.*, **110**, D11206, https://doi.org/10.1029/2004JD005293.

Ham, S.-H. and B. J. Sohn, 2010: Assessment of the calibration performance of satellite visible channels using cloud targets: application to Meteosat-8/9 and MTSAT-1R. Atmos. Chem. Phys., 10, https://doi.org/ 10.5194/acp-10-11131-2010.

——, S. Kato, F. G. Rose, 2019: Impacts of Partly Cloudy Pixels on Shortwave Broadband Irradiance Computations. *J. Atmos. Ocean. Technol.* **36,** 369–386, https://doi.org/10.1175/JTECH-D-18-0153.1.

Hou, W., Q. Yin, H. Xu, L. Li, Z. Chen, 2010: A comparison of two stream approximation for the discrete ordinate method and the SOS method, IGARSS, 2010, https://doi.org/10.1109/IGARSS.2010.5652681.

Irvine, W. M., 1968: Multiple-scattering by large particles. II. Optically thick layers. *Astrophys. J.*, **152**, 823–834.

Jin, Z., T. P. Charlock, W. L. Smith Jr., and K. Rutledge, 2004: A parameterization of ocean surface albedo. *Geophys. Res. Lett.*, **31**, L22301, https://doi.org/10.1029/2004GL021180.

Jin, Z., T. P. Charlock, P. Yang, Y. Xie, and W. Miller, 2008: Snow optical properties for different particle shapes with application to snow grain size retrieval and MODIS/CERES radiance comparison over Antarctica. *Rem. Sens. Environ.*, **112(9),** 3563–3581.

Joseph, J. H., W. J. Wiscombe, and J. A. Weinman, 1976: The Delta-Eddington Approximation for radiative flux transfer. *J. Atmos. Sci.*, **33**, 2452–2459.

Kato, S., T. P. Ackerman, J. H. Mather, and E. E. Clothiaux, 1999: The k-distribution method and correlated-k approximation for a shortwave radiative transfer model. *J. Quant. Spec. Radia. Trans.*, **62**, 109–121, https://doi.org/10.1016/S0022-4073(98)00075-2.

——, F. G. Rose, and T. P. Charlock, 2005: Computation of domain-averaged irradiance using satellite derived cloud properties. *J. Atmos. Ocean. Technol.*, **22**, 146–164, https://doi.org/10.1175/JTECH-1694.1.

——, N. G. Loeb, F. G. Rose, D. R. Doelling, D. A. Rutan, T. E. Caldwell, L. Yu, and R. A. Weller, 2013: Surface irradiances consistent with CERES-derived Top-of-atmosphere shortwave and longwave irradiances, 26, 2719–2740, https://doi.org/ 10.1175/JCLI-D-12-00436.1

——, F. G. Rose, D. A. Rutan, T. J. Thorsen, N. G. Loeb, D. R. Doelling, X. Huang, W. L. Smith, W. Su, and S.-H. Ham, 2018a: Surface irradiances of Edition 4.0 Clouds and the Earth's Radiant Energy System (CERES) Energy Balanced and Filled (EBAF) data product. *J. Climate*, **31**, 4501–4527, https://doi.org/10.1175/JCLI-D-17-0523.1.

——, F. G. Rose, S.-H. Ham, D. A. Rutan, A. Redkevich, T. E. Caldwell, S. Sun-Mack, W. F. Miller, and Y. Chen, 2018b: Radiative heating rates computed with clouds derived from satellite-based passive and active sensors and their effects on generation of available potential energy. *J. Geophys. Res., Submitted*.

Kawata, Y. and W. M. Irvine, 1970: The Eddington approximation for planetary atmospheres. *Astrophys. J.*, **160**, 787–790.

King, M. D. and Harshvardhan, 1986: Comparative accuracy of selected multiple scattering approximations. *J. Atmos. Sci.*, **43**, 784–801.

Kratz, D. P., and F. G. Rose, 1999: Accounting for molecular absorption within the spectral range of the CERES window channel. *J. Quant. Spec. Radia. Trans.*, **61**, 83–95, https://doi.org/10.1016/S0022-4073(97)00203-3.

Li, J.-L. F., D. E. Waliser, G. Stephens, S. Lee, T. L'Ecuyer, S. Kato, N. Loeb, H.-Y. Ma, 2013: Characterizing and understanding radiation budget biases in CMIP3/CMIP5 GCMs, contemporary GCM, and reanalysis. *J. Geophy. Res.*, **118(15)**, 8166–8184, https://doi.org/10.1002/jgrd.50378.

Liou, K.-N., 1974: Analytic two-stream and Four-stream Solutions for Radiative Transfer. *J. Atmos. Sci.*, **32**, 1473–1475.

——, Q. Fu, and T. P. Ackerman, 1988: A simple formulation of the delta-four-stream approximation for radiative transfer parameterizations. *J. Atmos. Sci.*, **45**, 1940–1948.

——, 1992: *Radiation and Cloud Processes in the Atmosphere: Theory, Observation, and Modeling*. Oxford University Press, 487 pp.

Liu, C., P. Yang, P. Minnis, N. Loeb, S. Kato, A. Heymsfield, and C. Schmitt, 2014: A two-habit model for the microphysical and optical properties of ice clouds. *Atmos. Chem. Phys.*, **14**, 13719–13737, https://doi.org/10.5194/acp-14-13719-2014.

Loeb, N. G., and Coauthors, 2018: Impact of ice cloud microphysics on satellite cloud retrievals and broadband flux radiative transfer model calculations. *J. Clim.*, **31,** 1851–1864, https://doi.org/10.1175/JCLI-D-17-0426.1.

Lu, P., H. Zhang, J. Li, 2009: A comparison of two-stream DISORT and Eddington radiative transfer schemes in a real atmospheric profile. *J. Quant. Spec. Radia. Trans.*, **110**, 129–138, https://doi.org/10.1016/j.jqsrt.2008.09.009.

McClatchey, R. A., R. W. Fenn, J. E. A. Selby, F. E. Volz, and J. S. Garing, 1972: *Optical Properties of the Atmosphere*. Air Force Cambridge Research Laboratory Environmental Research Paper 411, 3rd ed., pp. 110, Air Force Cambridge Research Laboratories, Bedford, MA.

Meador, W. E. and W. R. Weaver, 1980: Two-Stream Approximations to Radiative Transfer in Planetary Atmospheres: A Unified Description of Existing Methods and a New Improvement. *J. Atmos. Sci.*, **37**, 630–642.

Minnis, P.,W. L. Smith Jr., D. P. Garber, J. K. Ayers, and D. R. Doelling, 1995: *Cloud properties derived from GOES-7 for spring 1994 ARM intensive observing period using version 1.0.0 of ARM satellite data analysis program*. NASA Reference Publ. 1366, 59 pp.

——, and Coauthors, 2011a: CERES Edition-2 cloud property retrievals using TRMM VIRS and Terra and Aqua MODIS data—Part I: Algorithms. *IEEE Trans. Geosci. Remote Sens.*, **49**, 4374–4400, https://doi.org/10.1109/TGRS.2011.2144601.

——, and Coauthors, 2011b: CERES Edition-2 cloud property retrievals using TRMM VIRS and Terra and Aqua MODIS data—Part II: Examples of average results and comparisons with other data. *IEEE Trans. Geosci. Remote Sens.*, **49**, 4401–4430, https://doi.org/10.1109/TGRS.2011.2144602.

Pincus, R., and K. F. Evans, 2009: Computational cost and accuracy in calculating three-dimensional radiative transfer: Results for new implementations of Monte Carlo and SHDOM. *J. Atmos. Sci.*, **66**, 3131–3146, https://doi.org/10.1175/2009JAS3137.1.

Räisänen, P., 2002: Two-stream approximations revisited: A new improvement and tests with GCM data. *Quart. J. Roy. Meteoro. Soc.*, **128**, 2397–2416.

Rose, F. G., T. Charlock, Q. Fu, S. Kato, D. Rutan, and Z. Jin, 2006: CERES proto-edition 3 radiative transfer: Tests and radiative closure over surface validation sites. *12th Conference on Atmospheric Radiation*, American Meteorological Society, Madison, Wisconsin, 10–14 July 2006 [Available at http://snowdog.larc.nasa.gov/cave/].

——, D. A. Rutan, T. Charlock, G. L. Smith, and S. Kato, 2013: An algorithm for the constraining of radiative transfer calculations to CERES-observed broadband top-of-atmosphere irradiance. *J. Atmos. Ocean. Tech.*, **30**, 1091–1106, https://doi.org/10.1175/JTECH-D-12-00058.1.

Rutan, D. A., S. Kato, D. R. Doelling, F. G. Rose, L. T. Nguyen, T. E. Caldwell, and N. G. Loeb, 2015: CERES synoptic product: Methodology and validation of surface radiant flux. *J. Atmos. Oceanic Technol.*, **32**, 1121–1143, https://doi.org/ 10.1175/JTECH-D-14-00165.1.

Shettle, E. P. and J. A. Weinman, 1970: The transfer of solar irradiance through inhomogeneous turbid atmospheres evaluated by Eddington's approximation. *J. Atmos. Sci.*, **27**, 1048–1055.

Shibata, K., and A. Uchiyama, 1992: Accuracy of the delta-four-stream approximation in inhomogeneous scattering atmospheres. *J. Meteor. Soc. Japan,* **70(6)**, 1097–1109.

Stamnes, K., S.-C. Tsay, W. Wiscombe and K. Jayaweera, 1988: Numerically stable algorithm for discrete-ordinate-method radiative transfer in multiple scattering and emitting layered media. Appl. Opt. 27, 2502-2509.

Thom, H. C. S., 1958: A note on the gamma distribution. *Mon. Wea. Rev.*, **86,** 117–122.

Toon, O. B., C. P. McKay, and T. P. Ackerman, 1989: Rapid calculation of radiative heating rates and photodissociation rates in inhomogeneous multiple scattering atmospheres. *J. Geophys. Res.*, **94(D13)**, 16 287–16 301.

van de Hulst, 1974: The spherical albedo of a planet covered with a homogeneous cloud layer, *Astron. Astrophys.*, **35,** 209–214.

Wiscombe, W. J., 1977: The delta-M method: Rapid yet accurate radiative flux calculations for strongly asymmetric phase functions. *J. Atmos. Sci.*, **34**, 1408–1422.

Yang, P., G. W. Kattawar, G. Hong, P. Minnis, and Y. Hu, 2008a: Uncertainties associated with the surface texture of ice particles in satellite-based retrieval of cirrus clouds—Part I: Single scattering properties of ice crystals with surface roughness. *IEEE Trans. Geosci. Remote Sens.*, **46,** 1940–1947, https://doi.org/10.1109/TGRS.2008.916471.

——, G. Hong, G. W. Kattawar, P. Minnis, and Y. Hu, 2008b: Uncertainties associated with the surface texture of ice particles in satellite-based retrieval of cirrus clouds: Part II— Effect of particle surface roughness on retrieved cloud optical thickness and effective particle size.

IEEE Trans. Geosci. Remote Sens., **46,** 1948–1957, https://doi.org/10.1109/TGRS.2008.916472.

Zhang, F., Z. Shen, J. Li, X. Zhou, and L. Ma, 2012: Analytic Delta-Four-Stream Doubling-adding method for radiative transfer parameterizations. *J. Atmos. Sci.*, **70**, 794–808, https://doi.org/10.1175/JAS-D-12-0122.1.

——, and J. Li, 2013: Doubling–Adding method for delta-four-stream spherical harmonic expansion approximation in radiative transfer parameterization. *J. Atmos. Sci.*, **70**, 3084–3101.

Zhu, X. and A. Arking, 1994: Comparison of daily averaged reflection, transmission, and absorption for selected radiative flux transfer approximations. *J. Atmos. Sci.*, **51**, 3580–3592.

Table 1: Values of surface, atmospheric, cloud properties used for generating look-up-table (LUT) of SW irradiances and heating rates. The LUT is interpolated for the given cosine of solar zenith angle (μ_0) and cloud optical depth (τ_c) based on the method in Appendix B.

Input Variable	Value
Cosine of solar zenith angle (μ_0)	0.1 to 1.0 with a 0.1 interval
Surface types	Ocean, land, and snow
Atmospheric profiles	Midlatitude summer (MLS) and Midlatitude winter (MLW)
Cloud phases	Water (r_e = 10 μm) and ice (d_e = 65 μm) phases
Cloud optical depths (τ_c)	0.3, 1, 2, 5, 10, 20, 30, 40, and 50
Cloud top heights (CTHs)	1 km to 16 km with an 1 km interval
Cloud base heights (CBHs)	0 km to 15 km with an 1 km interval

Table 2: Annual means SW irradiances for various domains (global, ocean, land, Antarctic, and Arctic) computed by various radiative transfer methods (DISORT, D2strEdd, D2strQuad, and D4strQuad, and MC1M) with surface, cloud, and atmosphere properties derived for 2010. The numbers in parentheses are differences of the D2strEdd, D2strQuad, D4strQuad, and MC1M methods to the DISORT method.

	Domain				
Method	Global 90°S–90°N	Ocean 60°S–60°N	Land 60°S–60°N	Antarctic 90°S–60°S	Arctic 60°N–90°N
	TOA upward Irradiances (W m^{-2})				
DISORT	99.63	97.51	100.03	99.39	118.59
D2strEdd	99.06	96.82	99.72	98.85	118.28
	(–0.57)	(–0.69)	(–0.31)	(–0.54)	(–0.31)
D2strQuad	99.48	97.17	100.09	99.57	119.14
	(–0.15)	(–0.34)	(+0.06)	(+0.18)	(+0.56)
D4strQuad	99.96	97.87	100.25	99.74	118.88
	(+0.32)	(+0.36)	(+0.22)	(+0.34)	(+0.29)
MC1M	99.67	97.58	100.04	99.30	118.50
	(+0.04)	(+0.07)	(+0.01)	(–0.09)	(–0.09)
	Surface Downward Irradiances (W m^{-2})				
DISORT	186.54	195.80	210.91	99.45	103.71
D2strEdd	187.52	196.93	211.32	100.92	104.81
	(+0.98)	(+1.13)	(+0.41)	(+1.46)	(+1.09)
D2strQuad	188.44	197.61	212.31	102.40	107.12
	(+1.90)	(+1.81)	(+1.39)	(+2.95)	(+3.40)
D4strQuad	185.98	195.13	210.45	99.20	103.50
	(–0.56)	(–0.67)	(–0.46)	(–0.25)	(–0.21)
MC1M	186.41	195.73	210.64	99.31	103.59
	(–0.13)	(–0.08)	(–0.27)	(–0.15)	(–0.12)

Table 3: Computing time of the D2strEdd, D2strQuad, D4strEdd, MC1M, MC100M, and DISORT methods for the same set of cases (10 solar zenith angles × 3 surface types × 19 cloud cases × 2 atmospheric profiles, where the 19 cloud cases consist of 1 clear case + 9 cloud optical depths × 2 cloud phases). Note that computing time for Monte Carlo method depends on how many parallel modules are used. In this study, 70 parallel modules are used for independent computation of 70 gas absorption k bands. Since the computing time is also affected by the speed of the workstation, a normalized computing time by that of the D2strEdd method is provided in the second column.

Method	Computing time (sec)	Normalized time by D2strEdd
D2strEdd	11	1
D2strQuad	10	0.9
D4strQuad	19	1.7
MC10K	80	7.3
MC100K	792	72.0
MC1M	7847	713.3
MC10M	79515	7228.6
MC100M	946923	86083.9
DISORT 4str	7260	660.0
DISORT 8str	7282	662.0
DISORT 16str	7921	720.1
DISORT 24str	10205	927.7
DISORT 40str	36643	3331.2
DISORT 60str	42570	3870.0
DISORT 80str	52662	4787.5

Table C1: Changes of diurnally integrated biases of the D2strEdd, D2strQuad, and D4strQuad methods due to deviations of r_e, d_e, PW, and α_s. For diurnally-integrated biases, the three examples of solar zenith angles in Fig. 2 are used. When deviating r_e, d_e, and α_s, the fixed water vapor profile from MLS atmosphere (= 2.97 cm) is used. When deviating PW and α_s, ice clouds with d_e = 65 μm are used. When deviating r_e, d_e, and PW, the ocean surface type is used.

		Changes of biases in SW TOA upward irradiances (W m^{-2})		
Parameter x	Change of x	D2strEdd	D2strQuad	D4strQuad
Water r_e	8 → 10 μm	+0.51±0.42	+0.50±0.39	+0.55±0.42
Water r_e	10 → 17 μm	–0.45±0.24	–0.47±0.32	–0.38±0.22
Ice d_e	40 → 65 μm	+0.17±0.08	+0.16±0.08	+0.10±0.08
Ice d_e	65 → 80 μm	+0.02±0.04	+0.01±0.04	–0.02±0.03
PW	0.3 → 0.86 cm	+0.06±0.07	+0.18±0.03	+0.05±0.04
PW	2.97 → 5.87 cm	–0.08±0.10	+0.02±0.01	+0.04±0.03
α_s	0.1 → 0.36	+0.61±0.59	+0.23±0.58	–0.13±0.20
Parameter	Change of	Changes of biases in SW atmosphere-absorbed irradiances (W m^{-2})		
x	x	D2strEdd	D2strQuad	D4strQuad
Water r_e	8 → 10 μm	–0.09±0.08	+0.10±0.09	–0.09±0.06
Water r_e	10 → 17 μm	+0.02±0.10	–0.01±0.10	+0.02±0.03
Ice d_e	40 → 65 μm	–0.16±0.08	–0.16±0.08	–0.11±0.05
Ice d_e	65 → 80 μm	–0.01±0.02	–0.01±0.02	+0.01±0.02
PW	0.3 → 0.86 cm	+0.05±0.13	–0.14±0.05	–0.05±0.06
PW	2.97 → 5.87 cm	+0.24±0.19	+0.09±0.12	0.00±0.08
α_s	0.1 → 0.36	+0.15±0.16	–0.08±0.06	+0.04±0.04
Parameter	Change of	Changes of biases in SW surface downward irradiances (W m^{-2})		
x	x	D2strEdd	D2strQuad	D4strQuad
Water r_e	8 → 10 μm	–0.45±0.37	–0.42±0.34	–0.49±0.41
Water r_e	10 → 17 μm	+0.46±0.31	+0.51±0.42	+0.39±0.22
Ice d_e	40 → 65 μm	–0.01±0.04	+0.01±0.06	+0.01±0.02
Ice d_e	65 → 80 μm	–0.01±0.03	0.00±0.04	+0.01±0.01
PW	0.3 → 0.86 cm	–0.12±0.09	–0.05±0.08	0.00±0.04
PW	2.97 → 5.87 cm	–0.17±0.11	–0.12±0.13	–0.05±0.06
α_s	0.1 → 0.36	–0.39±0.76	+0.45±0.64	+0.10±0.16

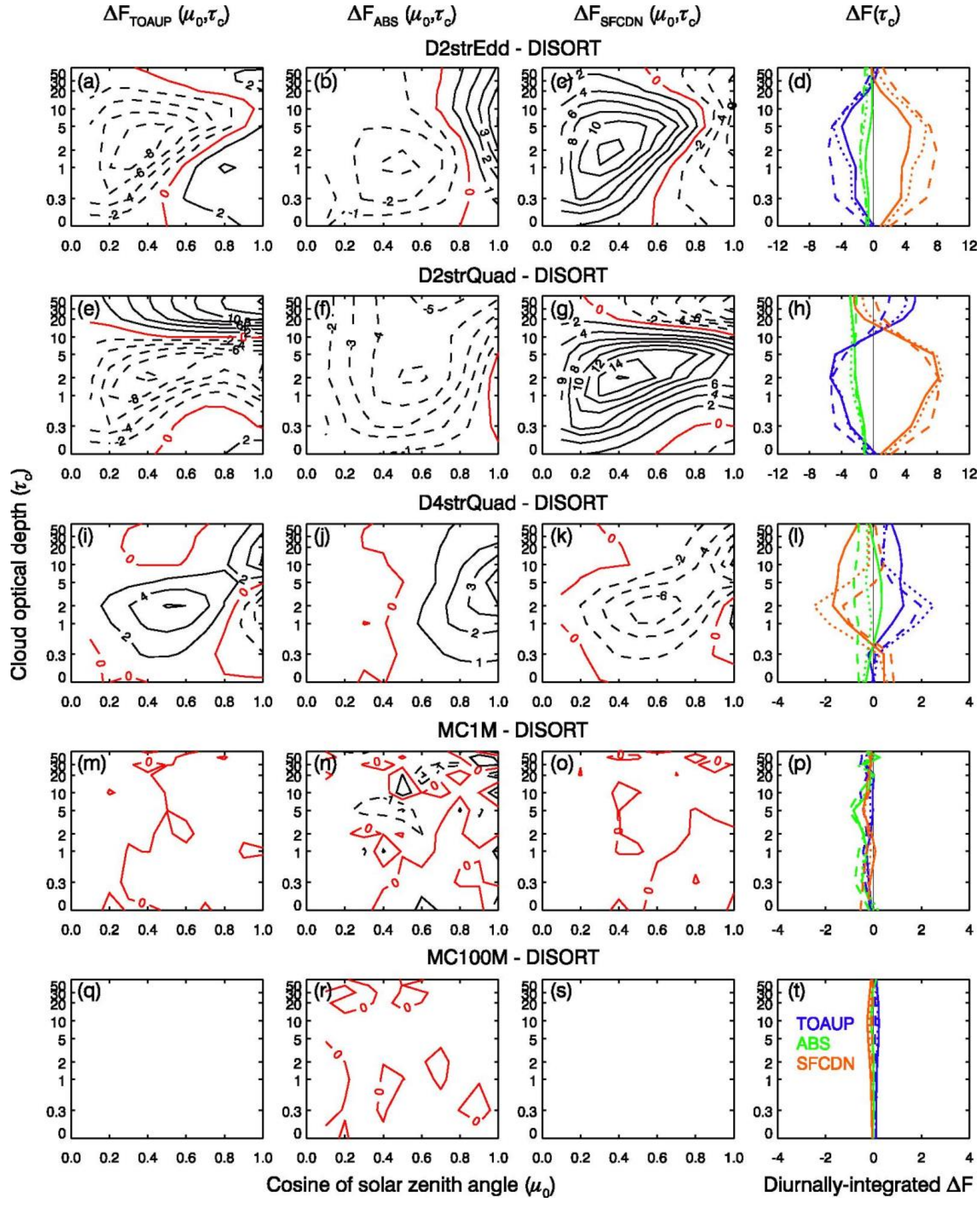

Figure 1: Biases of delta-two-stream-Eddington (D2strEdd) (the first row), delta-two-stream-Quadrature (D2strQuad) (the second row), delta-four-stream-quadrature (D4strQuad) (the third row), MC with 10^6 photons (MC1M) (the fourth row), and MC with 10^8 photons (MC100M) (the fifth row) to the DISORT simulation results with 40 streams. Instantaneous biases as a function

of cosine of solar zenith angle (μ_0) and cloud optical depth (τ_c) are given for TOA upward (the first column), atmosphere-absorbed (the second column), and surface downward (the third column) SW irradiances. In the first to third columns, solid contour lines are positive values, and dashed lines are negative values. Zero lines are given as red lines. The intervals of contours for TOA upward (the first column), atmosphere-absorbed (the second column), and surface downward (the third column) irradiances are 2, 1, and 2 W m^{-2}, respectively. Using the three examples of diurnal variations of μ_0 in Fig. 2 (solid, dashed, and dotted lines), the instantaneous biases are integrated for TOA upward (blue), atmosphere-absorbed (green), and surface downward (orange) irradiance (the four column). The simulation is performed for water clouds over ocean with the mid-latitude summer (MLS) profile. Cloud top and base heights of the water cloud layer are, respectively, 2 and 3 km. Water particle effective radius of 10 μm is used.

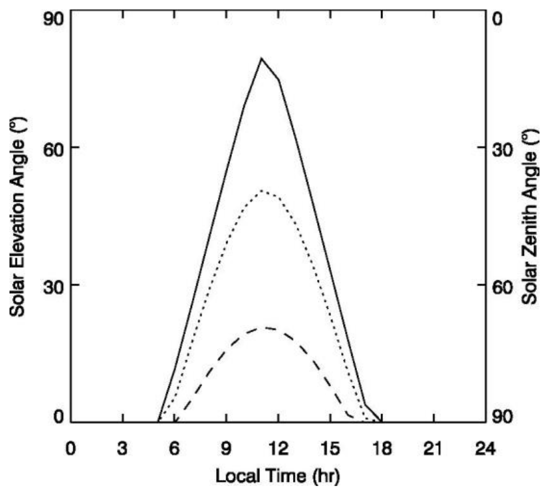

Figure 2: Examples of diurnal variations of the solar zenith angle on 15th October 2010. Three locations are selected; 1) 0.5°E, 0.5°N (solid line), 2) 0.5°E, 30.5°N (dotted line), and 3) 0.5°E, 60.5°N (dashed line). SYN Ed4A hourly product is used to obtain the solar zenith angles.

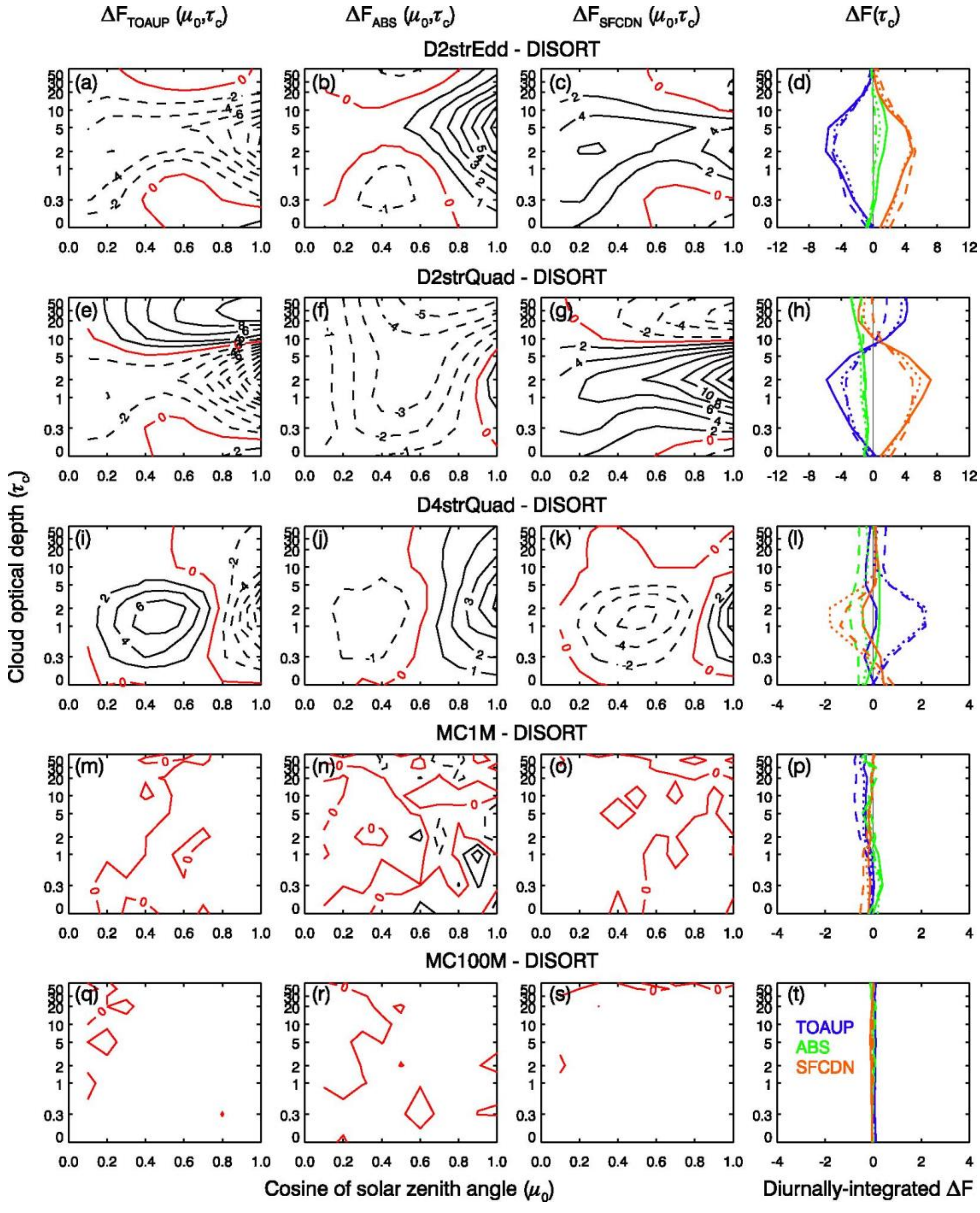

Figure 3: Same as Fig. 1 but for ice clouds. Cloud top and base heights of the ice cloud layer are, respectively,10 and 12 km. The ice particle effective diameter of 65 μm is used.

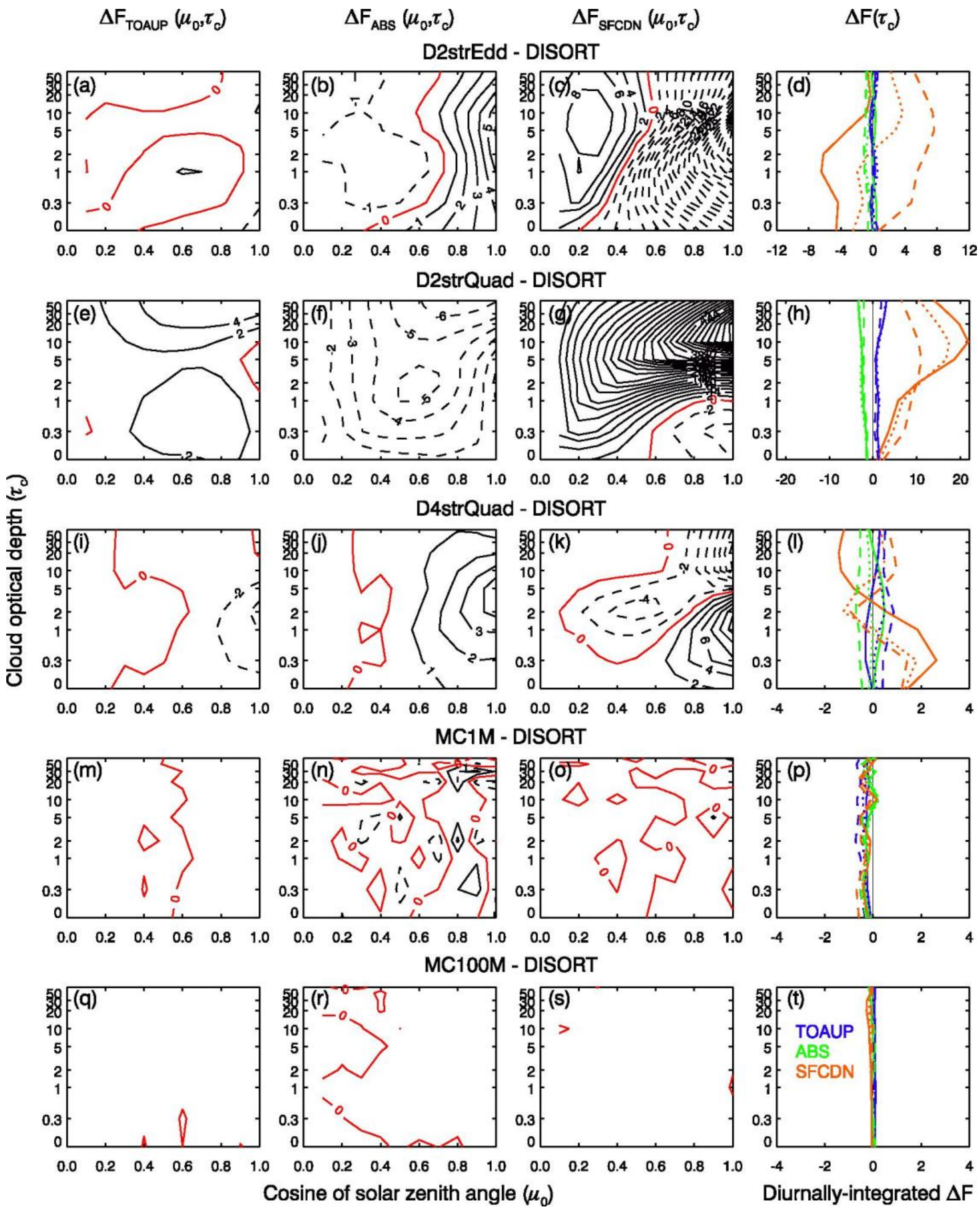

Figure 4: Same as Fig. 1 but for water clouds over the snow surface type.

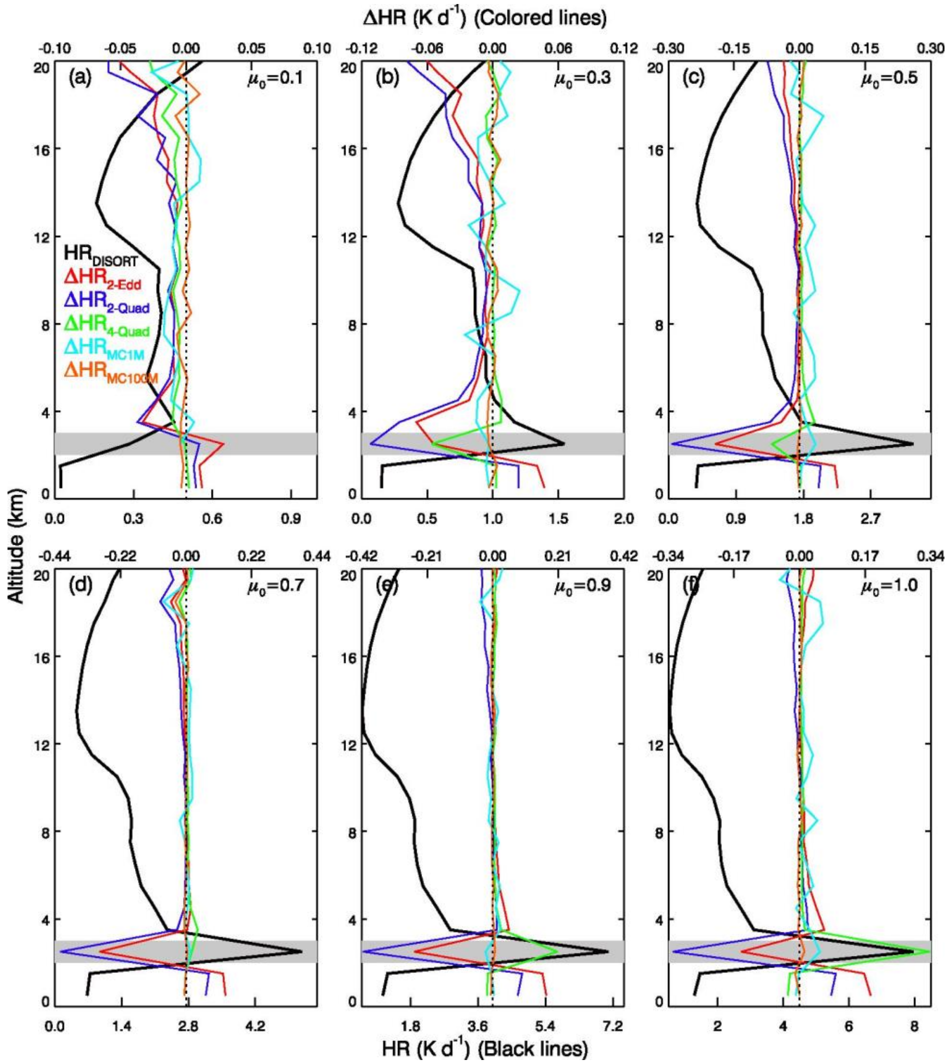

Figure 5: Computed SW heating rate profiles (black lines) by the 40-stream DISORT method with a cosine of solar zenith angle (μ_0) of (a) 0.1 (b) 0.3 (c) 0.5 (d) 0.7 (e) 0.9 (f) 1.0 for water clouds over ocean. Cloud top and base heights of the water cloud layer are, respectively, 2 and 3 km (gray box area). The water particle effective radius of 10 μm and cloud optical depth of 10 are used. Mid-latitude atmospheric (MLS) profiles are used for temperature and humidity profiles. The biases in SW heating rates by the D2strEdd (red lines), D2strQuad (blue lines), D4strQuad (green lines), MC1M (cyan lines), and MC100M (orange lines) methods are given with the top horizontal axes where DISORT results are used as references. Note that the magnitude of biases is one order smaller than the absolute magnitude of the MC heating rates.

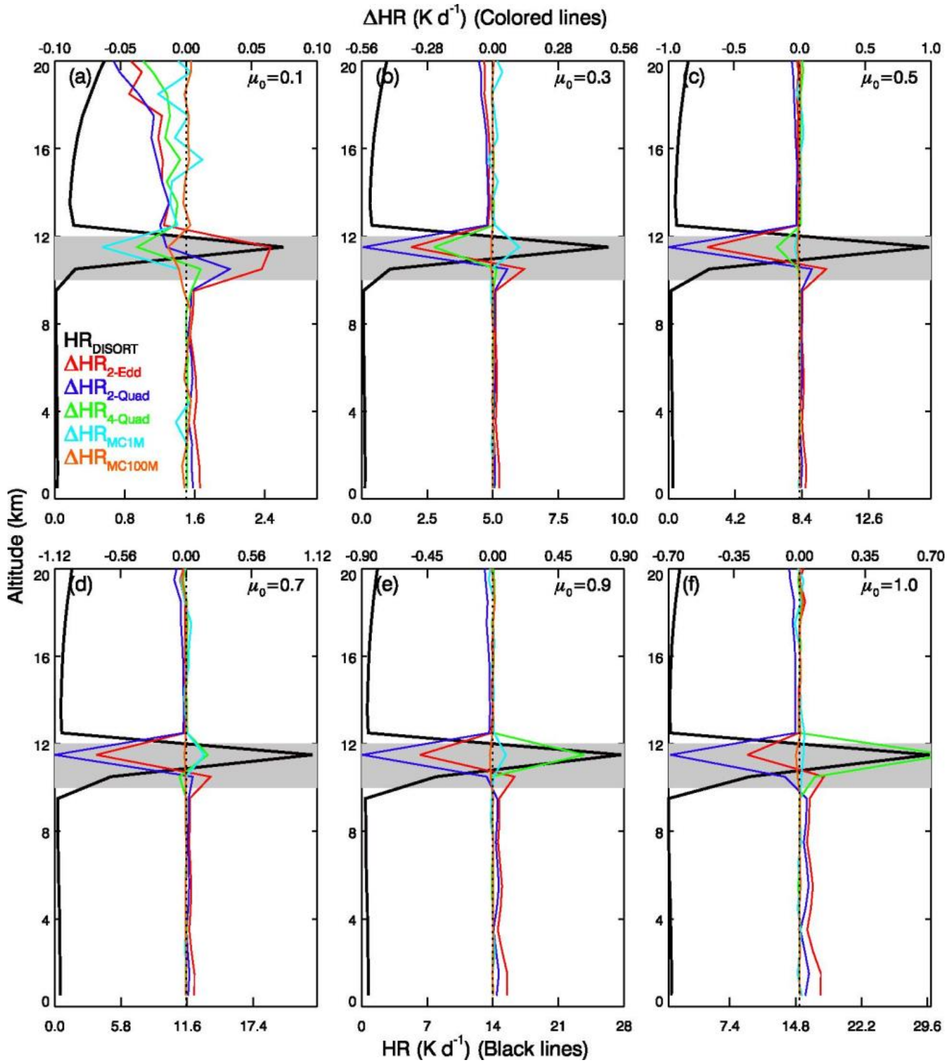

Figure 6: Same as Fig. 5 but for ice clouds with a cloud optical depth of 10, ice effective diameter = 65 μm, cloud base height = 10 km, and cloud top height = 12 km.

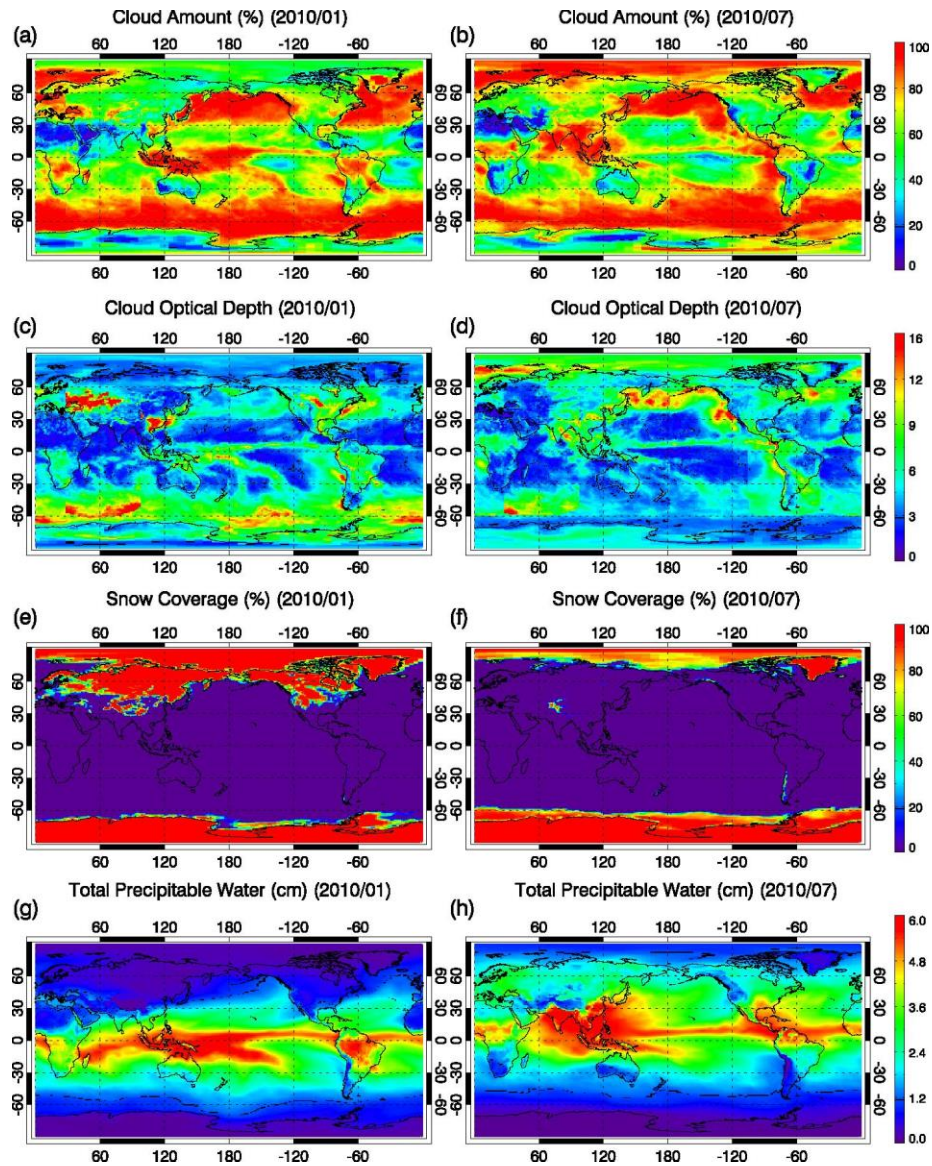

Figure 7: Monthly mean cloud amounts (%) for (a) January 2010 and (b) July 2010. (c) and (d) are the same as (a) and (b) but for cloud optical depths. (e) and (f) are the same as (a) and (b) but for snow/ice coverage (%). (g) and (h) are the same as (a) and (b) but for total precipitable water (cm).

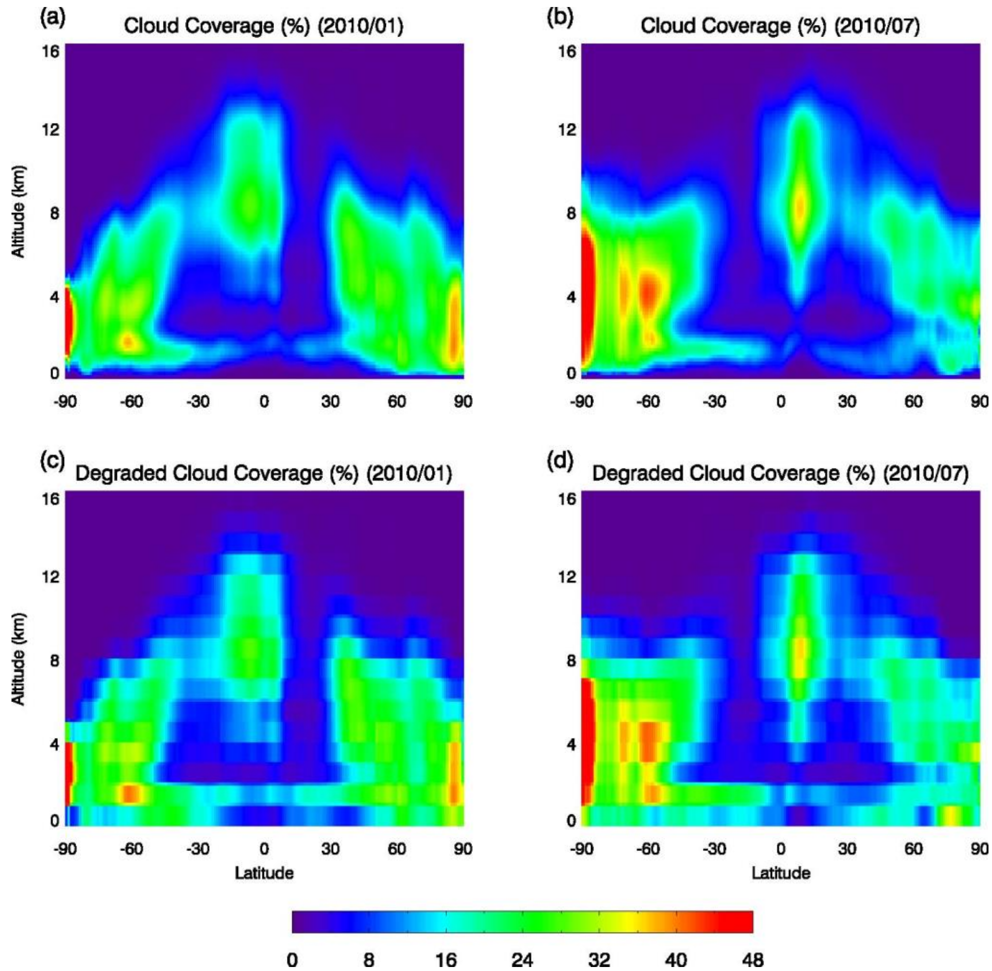

Figure 8: Monthly mean volume cloud coverage (%) profiles from 0 to 20 km computed with a 0.16 km vertical grid bin interval for (a) January 2010 (b) July 2010. In each 1° grid box, cloud base and top heights of four cloud types (high, mid-high, mid-low, and low) are used to assign the cloud coverage profile. Then the cloud coverage profiles are temporally and zonally averaged to plot this figure. Since the discretized cloud top and base heights are used in applying the look-up table (LUT), the cloud coverages with the discretized cloud heights are also provided in (c) January 2010 (d) July 2010.

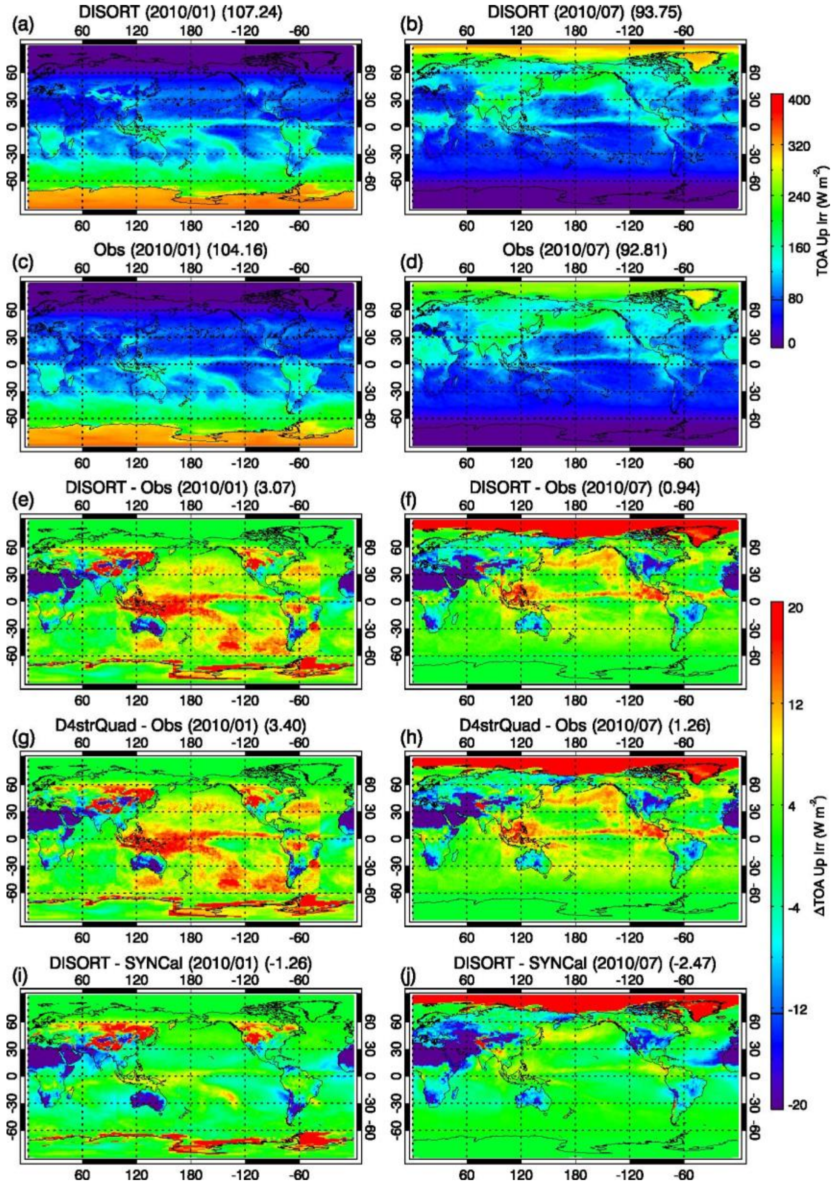

Figure 9: Monthly mean TOA SW irradiances computed with the DISORT method using simplified surface, atmosphere, and cloud properties for (a) January 2010 (b) July 2010. (c) and (d) are the same as in (a) and (b) but for observed TOA SW irradiances from CERES SYN product. The differences between DISORT-computed and observed irradiances are provided for (e) January 2010 (b) July 2010. (g) and (h) are same as in (e) and (f) but for differences between D4strQuad-computed and observed irradiances. Differences between DISORT-computed

irradiances (from our study) and SYN calculated irradiances (from CERES SYN product) are obtained for (a) January 2010 and (b) July 2010.

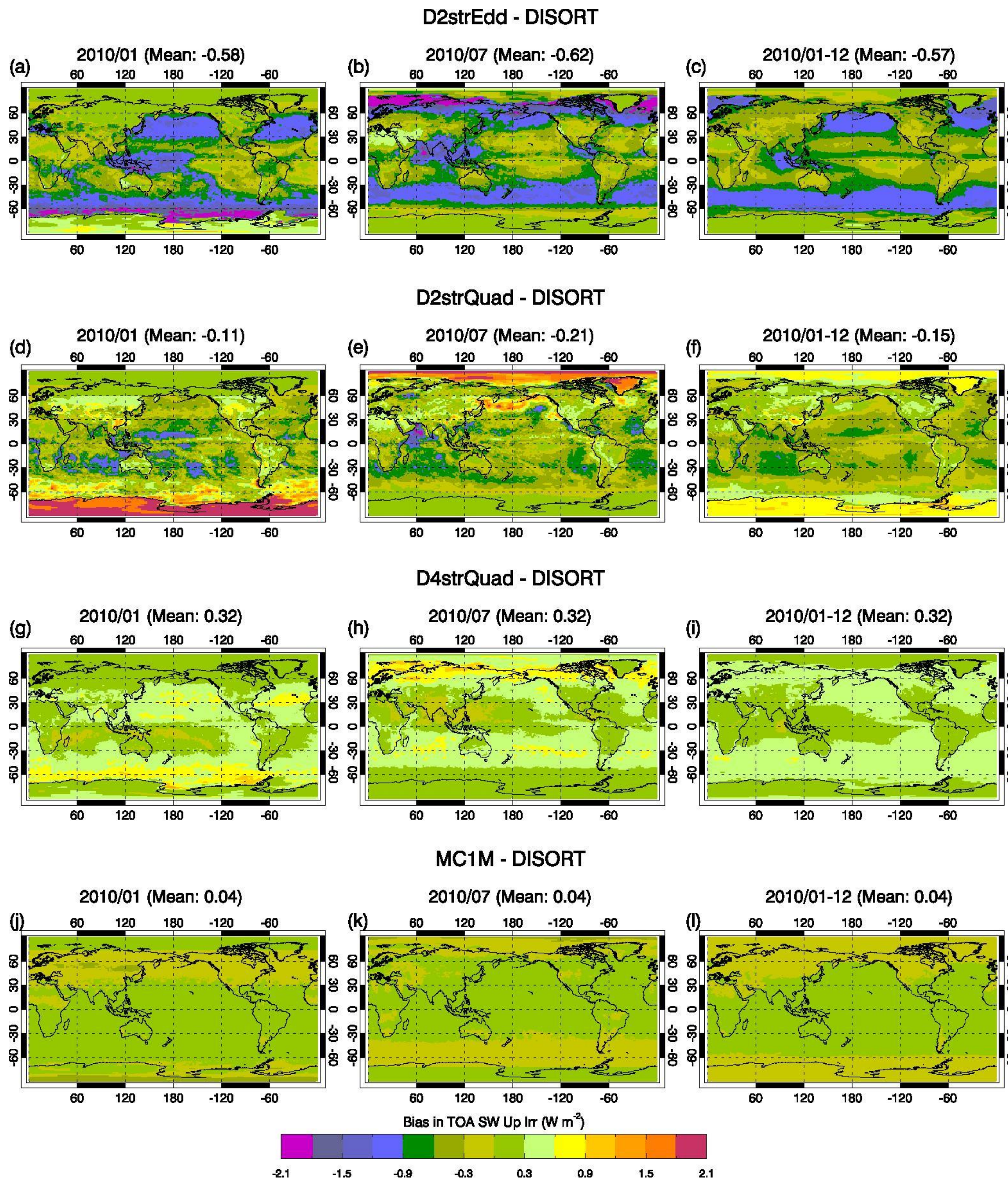

Figure 10: Biases in SW TOA upward irradiances (W m^{-2}) by the D2strEdd (the first row) D2strQuad (the second row) D4strQuad methods (the third row), and MC1M (the forth row) methods to the 40-stream DISORT method. The biases are obtained for January 2010 (left column), July 2010 (middle column), and January–December 2010 (right column). Numbers in parentheses are global means.

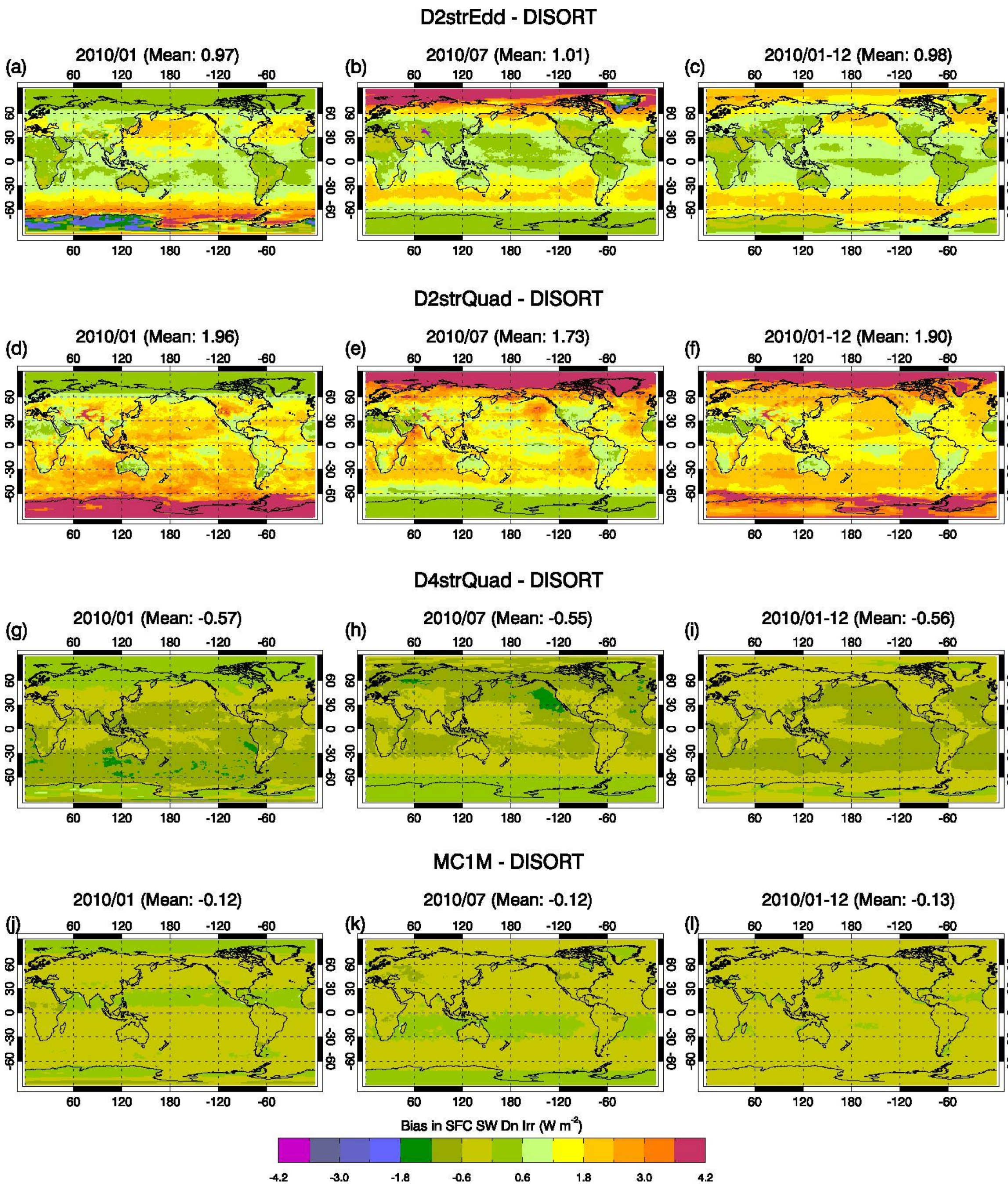

Figure 11: Same as Fig. 10 but for biases in surface downward irradiances (W m^{-2}).

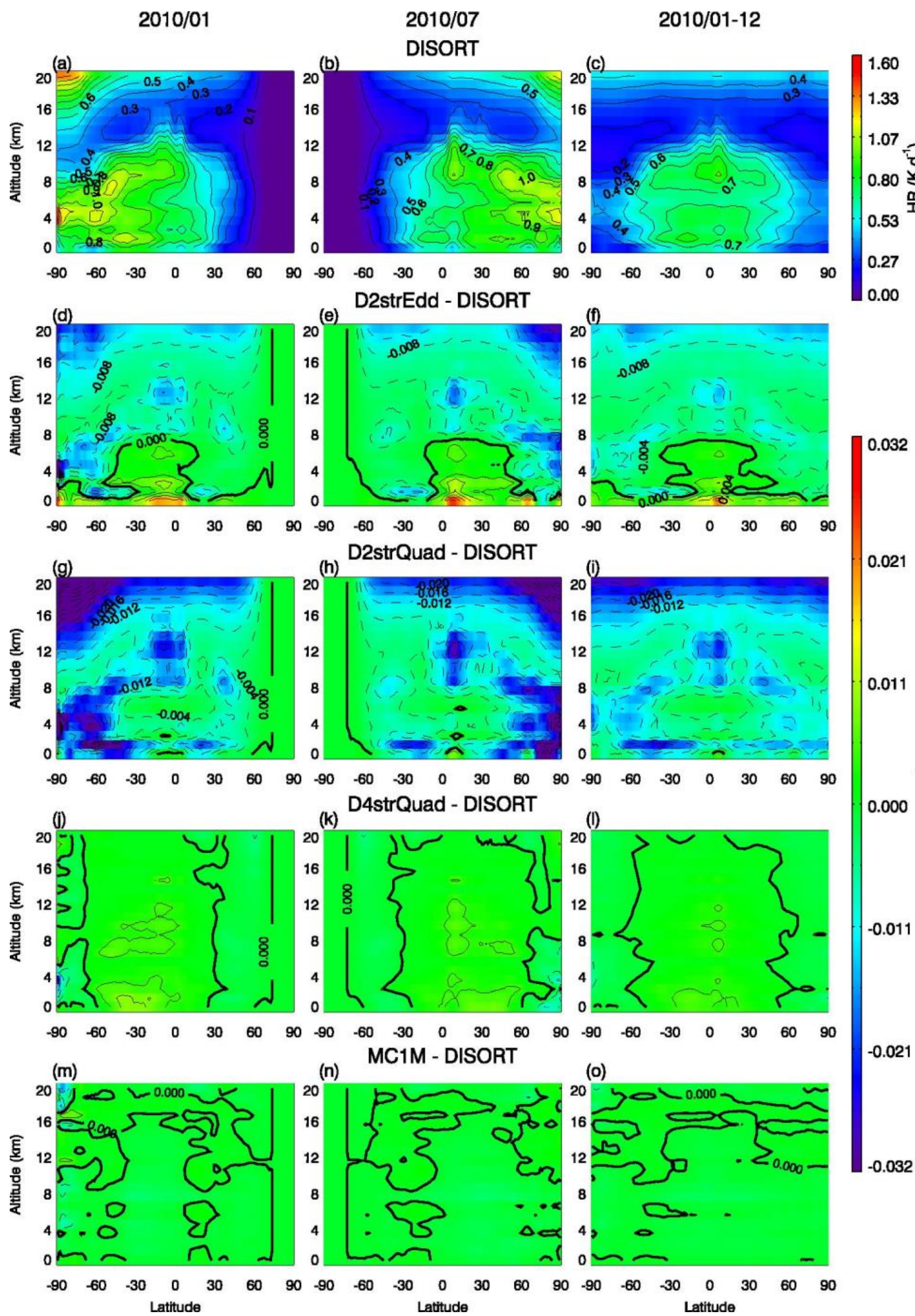

Figure 12: SW heating rates computed by the DISORT method for (a) January 2010 (b) July 2010 (c) January–December 2010. Biases in SW heating rates by the D2strEdd method in comparison to the DISORT method for (d) January 2010 (e) July 2010 (f) January–December 2010. (g)–(i) are the same as (d)–(f) but for biases by the D2strQuad method. (j)–(l) are the same

as (d)–(f) but for biases by the D4strQuad method. (m)–(o) are the same as (d)–(f) but for biases by the MC1M method. The contour interval is 0.1 K d^{-1} for (a)–(c) and 0.004 K d^{-1} for (d)–(o). Thick solid black lines in (d)–(o) are zero lines.

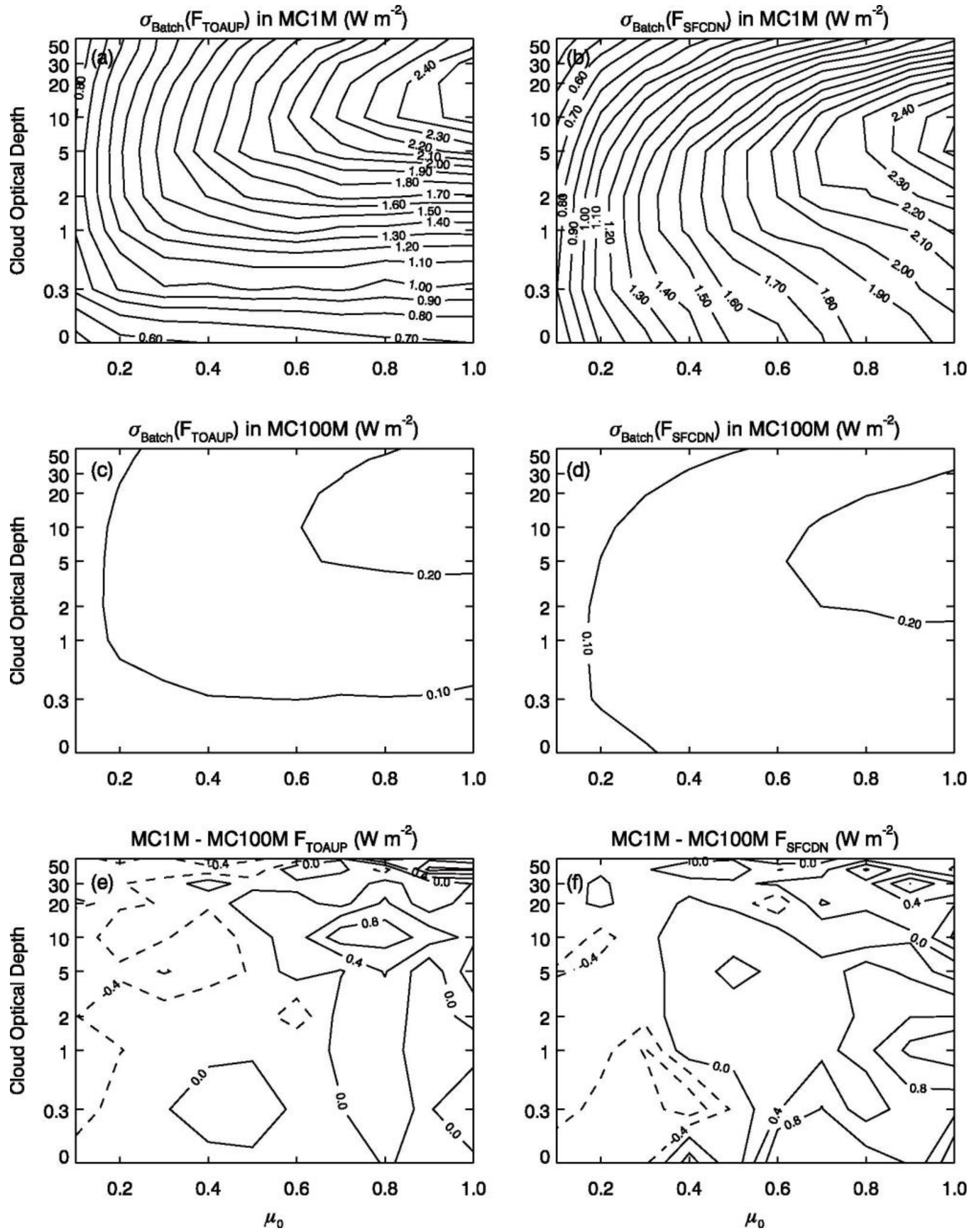

Figure A1: Standard deviations (σ_{Batch}) of (a) TOA upward SW irradiances (b) surface downward SW irradiances computed by the MC method with 10^6 photons (MC1M). (c) and (d) are the same as (a) and (b) except that 10^8 photons are used (MC100M). Differences in (e) TOA upward SW irradiances (f) surface downward SW irradiances computed from 10^6 and 10^8 photons (MC1M minus MC100M). Water clouds located at 2–3 km over ocean are placed in the

Midlatitude-summer profile (MLS) atmosphere. The interval of contour lines is 0.1 W m^{-2} in (a)–(d) and 0.4 W m^{-2} in (e)–(f).

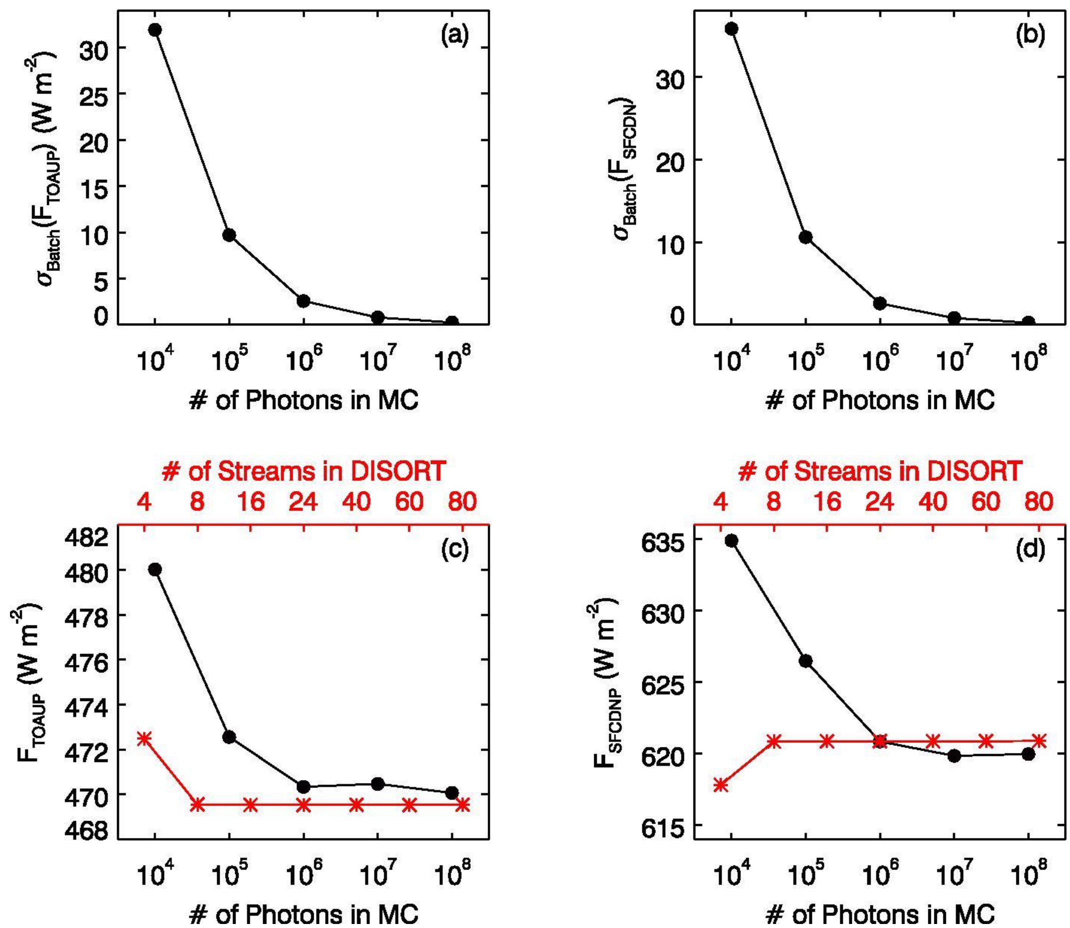

Figure A2: Standard deviations (σ_{Batch}) of (a) TOA upward SW irradiances and (b) surface downward SW irradiances for various numbers of photons in the MC method. The results of the MC method (black symbols and lines) with various numbers of photons are compared with those from the DISORT method (red symbols and lines) with various number of streams for (c) TOA upward SW irradiances and (d) surface downward SW irradiances. The cosine of solar zenith angle (μ_0) = 1.0 and cloud optical depth = 10 are used for the simulations. Water clouds located at 2–3 km over ocean are placed in the Midlatitude-summer profile (MLS) atmosphere.

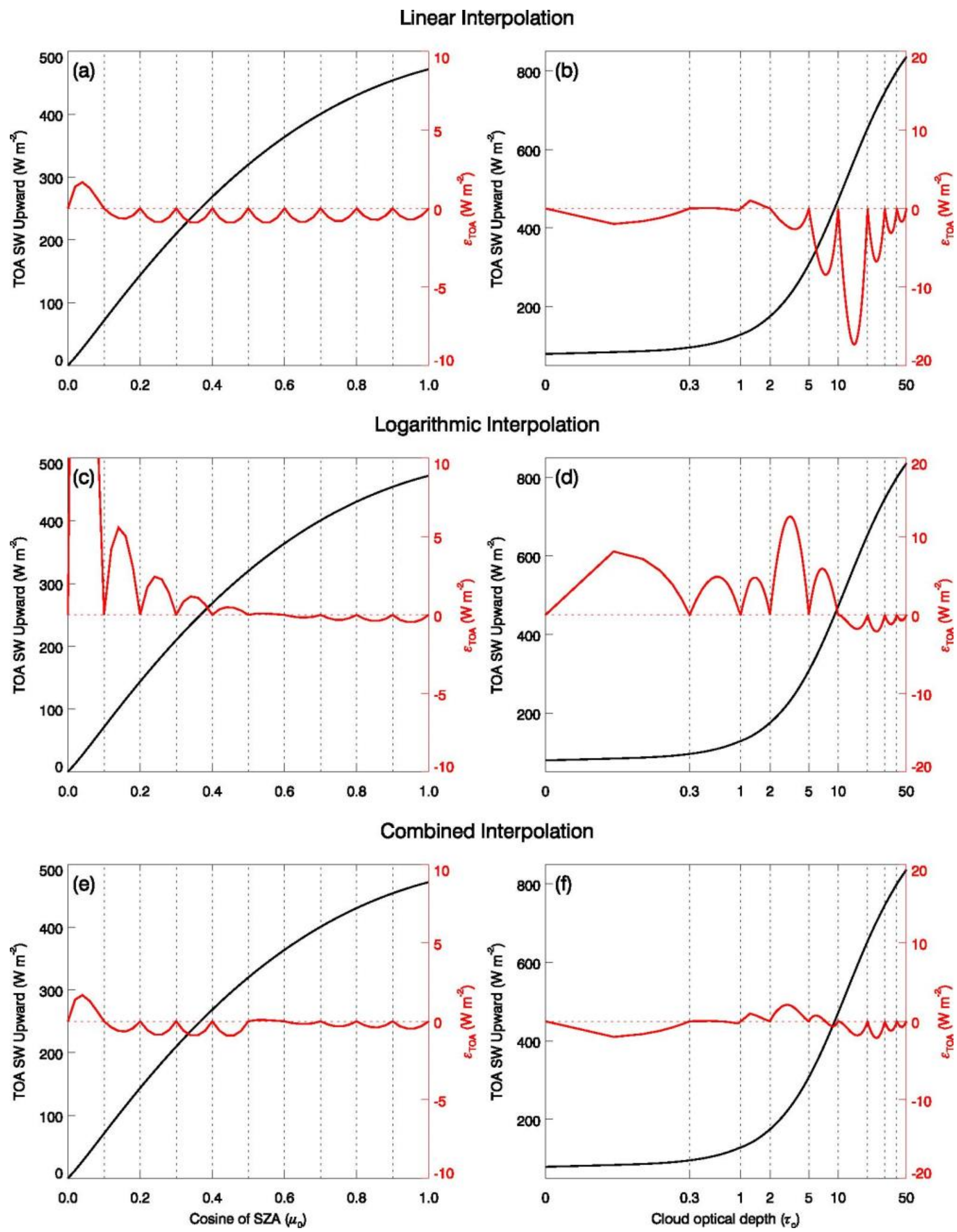

Figure B1: Black lines are SW TOA irradiances as a function of cosine of solar zenith angle (μ_0) with τ_c = 10 (left column) and cloud optical depth (τ_c) with μ_0 = 1 (right column). Red lines are interpolation errors (ε_{TOA}) when the linear (the first row), logarithmic (the second row), and combined interpolation (the third row) are used. The combined method is described in Appendix B. Vertical dashed lines are cosine of solar zenith angle (left column) or cloud optical depth (right column) bins used in the look-up-table (LUT).

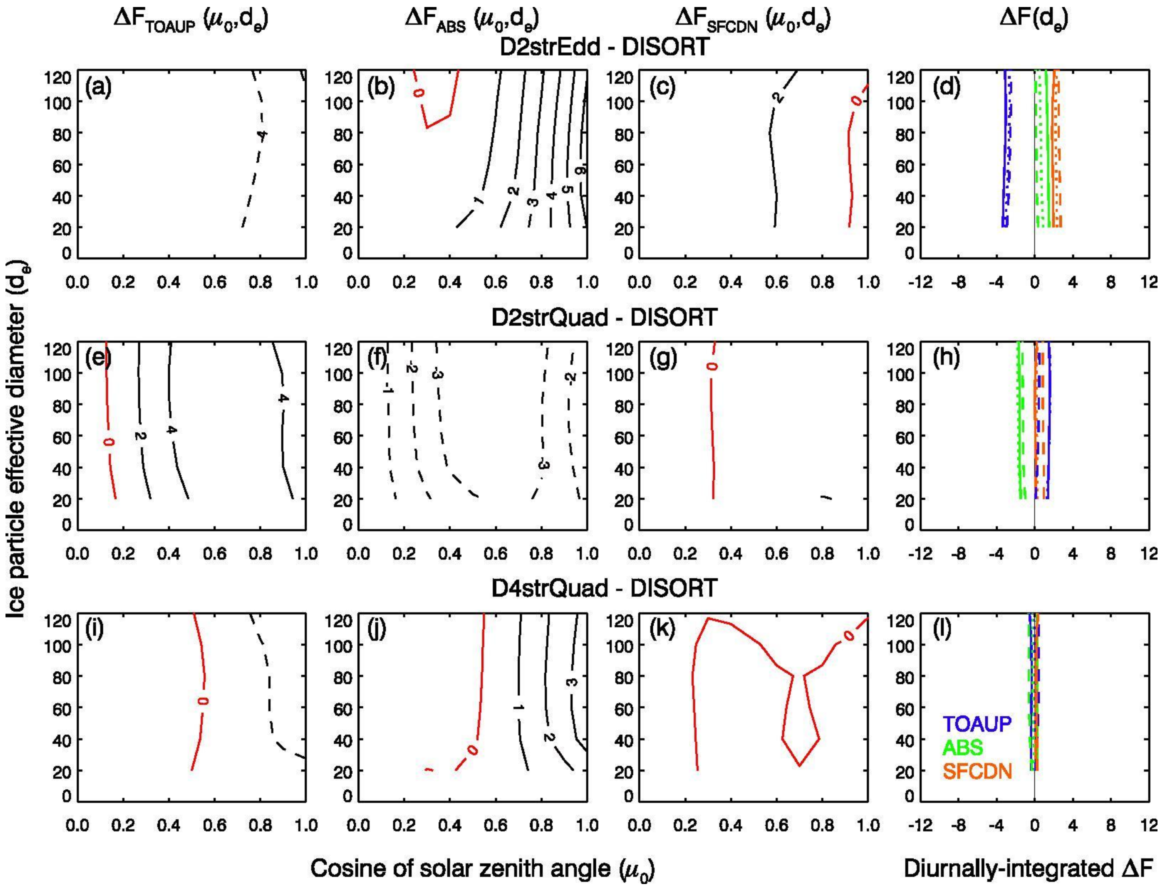

Figure C1: Same as Fig. 3 but for instantaneous biases as a function of the cosine of solar zenith angle (μ_0) and ice particle effective diameter (d_e) are given for TOA upward (the first column), atmosphere-absorbed (the second column), and surface downward (the third column) SW irradiances. Using the three examples of diurnal variations of μ_0 in Fig. 2 (solid, dashed, and dotted lines), the instantaneous biases are integrated for TOA upward (blue), atmosphere-absorbed (green), and surface downward (orange) irradiance in the four column. The simulation is performed for ice clouds over ocean with the mid-latitude summer (MLS) profile. Cloud top and base heights of the cloud layer are 10 and 12 km, respectively. The cloud optical depth of 10 is used. The unit of biases is W m^{-2}.

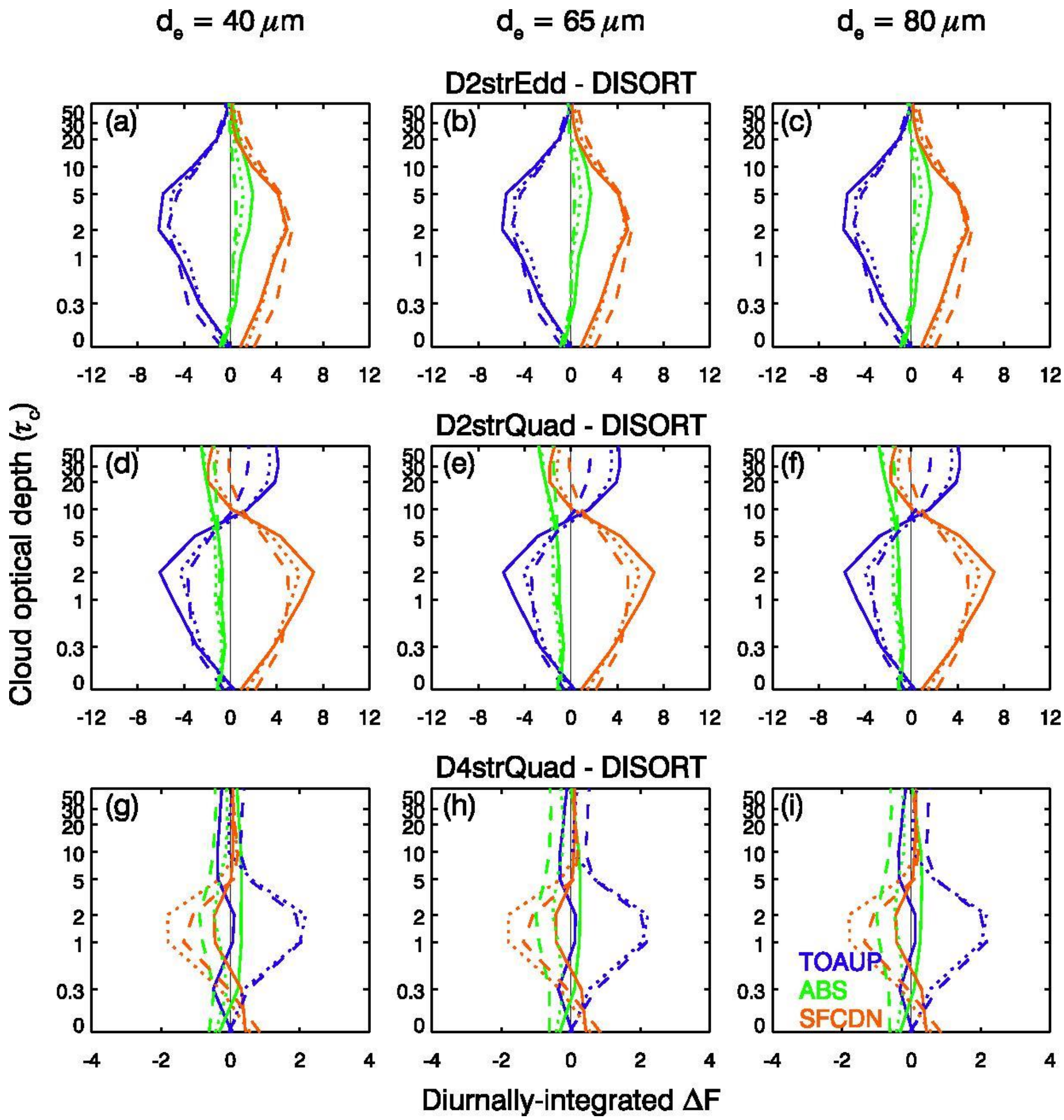

Figure C2: Diurnally-integrated biases in TOA upward (blue lines), atmosphere-absorbed (green lines), and surface downward (orange lines) irradiances using the three examples of cosine of solar zenith angle (μ_0) variations in Fig. 2. Three ice effective diameter (d_e) values as = 40 μm (left column), 65 μm (middle column), and 80 μm (right column) are used over ocean. The biases of the D2strEdd, D2strQuad, and D4strQuad methods are given in the first, second, and third row, respectively. Ice clouds at 10–12 km in MLS atmosphere are considered. The unit of biases (ΔF) is W m^{-2}.

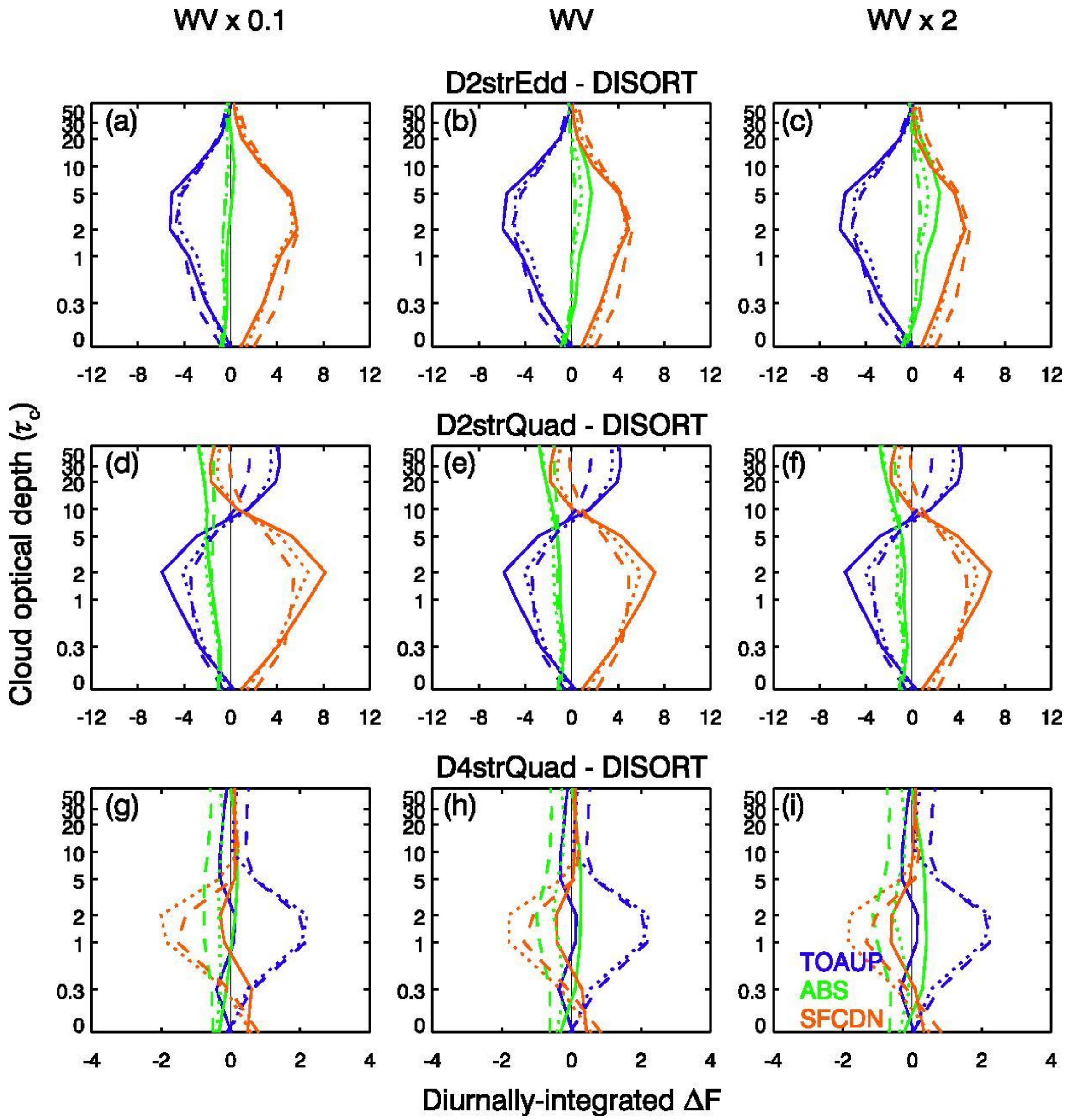

Figures C3: Same as Fig. C2 but for three different water vapor profiles as MLS water vapor profile scaled by 0.1 (left column), MLS water vapor profile (middle column), and MLS water vapor profile scaled by 2 (right column). Ice clouds with a particle size of d_e= 65 μm and 10–12 km altitude are assumed over ocean. The unit of biases (ΔF) is W m^{-2}.

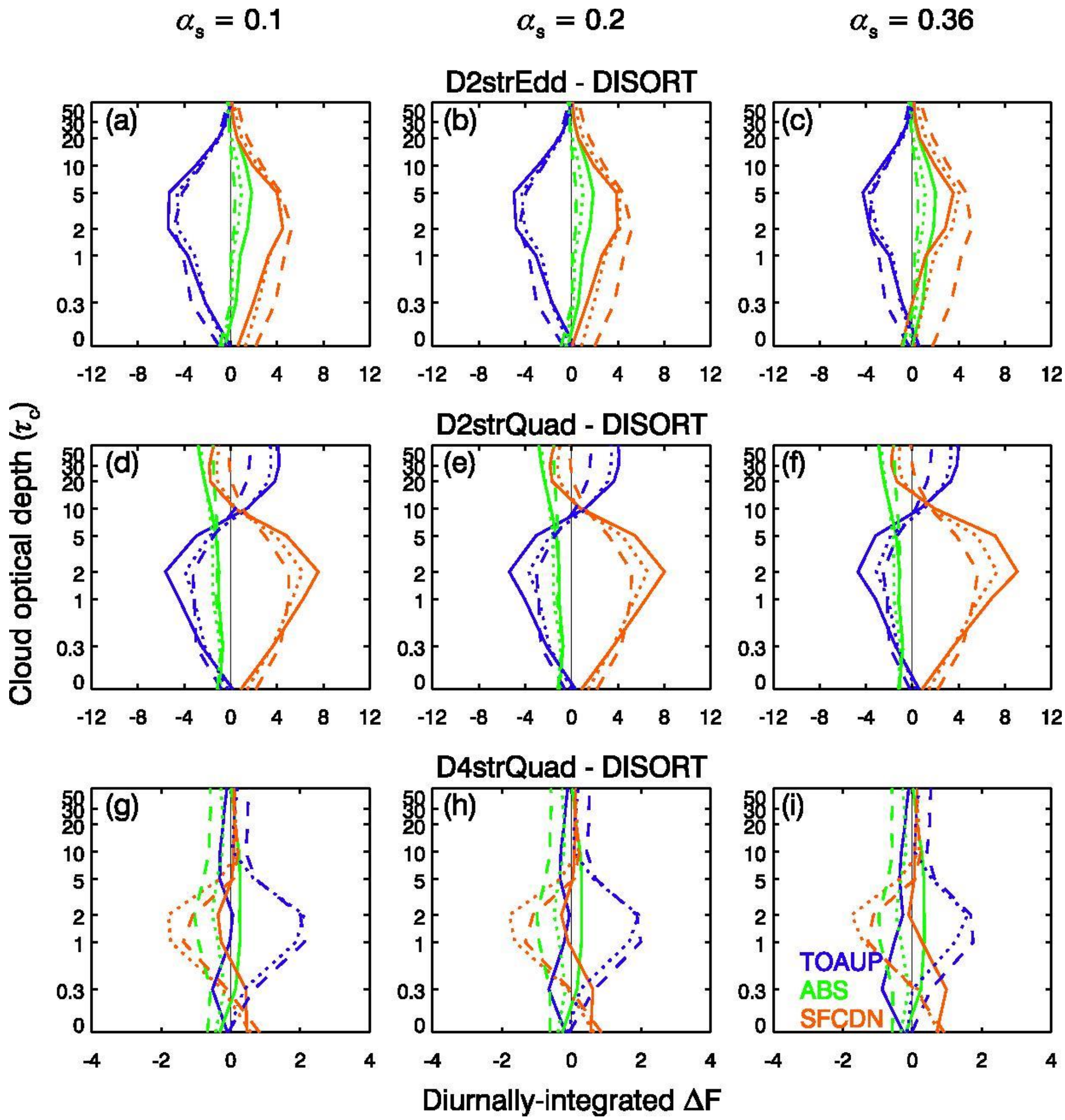

Figure C4: Same as in Fig. C2 but for three different land surface albedos (α_s) as 0.1 (left column), 0.2 (middle column), and 0.36 (right column). Ice clouds with a particle size of d_e= 65 μm and 10–12 km altitude are assumed over ocean in MLS atmosphere. The unit of biases (ΔF) is W m^{-2}.